Department of Precision and Microsystems Engineering

Design of a Compliant Hinge based on Closed Form Pressure Balancing

R.F.P. Gomes

Report no   : 2020.012
Coach   : ir. J.P.A. Nijssen
Professor   : dr. ir. R.A.J. van Ostayen
Specialisation : Mechatronic System Design
Type of report : MSc. Thesis
Date   : 2 March 2020

TUDelft   Delft University of Technology

Challenge the future

Design of a Compliant Hinge

based on Closed Form Pressure Balancing

by

R.F.P. Gomes

to obtain the degree of Master of Science
at the Delft University of Technology,
to be defended publicly on Monday March 2, 2020 at 1:30 PM.

This thesis is confidential and cannot be made public until March 2, 2022.

An electronic version of this thesis is available at `http://repository.tudelft.nl/`.

TUDelft

Preface

This document presents the final result of my study High-Tech Engineering here at the TU Delft, at the faculty of Mechanical, Maritime and Material Engineering (3mE).

First and foremost, I would like to thank my daily supervisor Joep Nijssen for guiding me during this project. Our several meetings and interesting discussions proved to be crucial for the results of this research. I really appreciate the time and effort you have put in my personal development, as well as the development of the project.

My interest in engineering stated when I was younger, taking things apart to see how they were constructed. Helping multiple people in my surroundings to solve mechanical problems in various applications. Back then I would have never expected a master degree in such a comprehensive technical discipline. I am incredibly grateful for all the support over the years and especially during this last year.

Furthermore, I would like to thank Ron van Ostayen for all the constructive feedback and sharp questions to enhance the quality of the project. Also I want to thank my fellow PME students for their input and insights during our group meetings on Wednesday as well as outside the meetings.

I want to thank the entire technical support staff of PME, especially Patrick van Holst, Bradley But and Rob Luttjeboer for their help with my experiments and experimental test setup. Moreover, I would also like to thank Rick, Luuk & Vincent for reviewing my work. Finally, a big compliment to my parents, sisters and friends for supporting me throughout these years in every way possible. It has been a great experience.

Robin Gomes
Delft, March 2020

Contents

1

Introduction

1.1. Background information

Many applications require rotation with constant velocity, such as power transmission systems, parallel robot manipulators, rehabilitation and medical devices [1–3]. The conventional method to solve the problem of rotational transmission is a rigid-body configuration. However, rigid-body configurations have many disadvantages, such as wear, friction, backlash, the need for maintenance and they are generally cost ineffective [4]. Besides they sometimes work inside a vacuum, wet or dirty environment. Making it difficult to use conventional bearings as pivot point, due to the need for lubrication [5]. Currently engineering applications were high positioning accuracy is required are popular, such as the scanning tunneling microscopes, precision positioning stages, X-ray lithography, and wafer alignment in microlithography [6–8]. The backlash in the rigid-body mechanical connections is a problem for the needed accuracy of these applications. To overcome this problem, compliant mechanisms can be used.

Compliant mechanisms transfer motion, force or energy by using the elastic deformation of its flexure joints [9]. Compliant mechanisms are cheaper to fabricate than conventional types of high precision mechanisms which feature rigid joints [5]. They could easily be fabricated as a monolithic structure due to its hinge-less design. The monolithic design reduces wear, friction, and backlash in the mechanism and correspondingly increases precision, which is vital in the design of high-precision instrumentation [10]. The input energy is not directly transferred to the output of the mechanism, as on deformation the energy is stored and thereby conserved in elastic members without dissipation [11].

Flexure hinges are usually constrained to a single-axis rotation and are widely utilized in precision positioning applications [12]. However, they usually have a limited range of motion constrained to a few radians, and a limited load capacity [13, 14]. Potentially, many more applications could benefit from similar mechanisms if they possessed a larger range motion and higher load capacities. This has resulted in more complex flexure designs (e.g. [15, 16]) or an increased number of joints in the mechanism (e.g. [17, 18]). The majority of compliant hinges are designed using solely solid elements. However, mechanical machine components have also been investigated that make use of the properties of fluids to obtain a desired behaviour. Examples are, dampers to relocate energy from a dynamic system, concept compliant bearings supports and aerostatic dampers [19–21]. These concepts make use of an encapsulated fluid. The use of a fluid inside a boundary material could be introduced for the realization of a new compliant hinge design, improving the state of the art compliant hinges.

1.2. Project objective

As mentioned before, literature learns us that conventional compliant hinges have limited range of motion and load capacity for deformation. To enlarge the potential of these hinges the range of operation should be increased. The range of operation is defined as the stiffness discrepancy between the normal- and rotation-stiffness. To make a sufficient comparison, the stiffness magnitudes of the compliant hinge should be in the same order of magnitude as the average stiffness magnitude of the conventional complaint hinges, therefore the rotational stiffness of the proposed hinge needs to be reduced while increasing the support stiffness. The resulting hinge should desirably have a high normal-to-rotation stiffness ratio. To compare the proposed compliant hinge to the conventional compliant hinges, the performance is expressed by the stiffness ratio between the normal- and rotation-stiffness. The performance of the proposed compliant hinge should exceed the performance of the conventional compliant hinges, as the individual stiffness magnitudes are within a set of boundary conditions. The main objective of this thesis project is set as follows,

Design a compliant hinge which has a higher performance than the conventional compliant hinges.

In order to improve the performance of the proposed compliant hinge, knowledge about the fundamental working principles of a closed fluid cell have to be obtained first. Next, the design of the compliant hinge should be obtained along with the realization of the demonstrator. Finally, an experimental test setup has to be built and experiments have to be conducted in order to validate if the performance of the proposed compliant hinge exceeds the performance of conventional compliant hinges.

1.3. Thesis outline

This thesis starts by describing the fundamental theory behind the working principles of a compliant hinge, based on a closed form pressure balancing, in Chapter 2. Chapter 3 elaborates on the boundary conditions, the design choices and the detailed design of the hinge as well as the measurement results found in this thesis. The main part of this thesis is found in the paper: "*Design of a Compliant Hinge based on Closed Form Pressure Balancing*" that is presented in Chapter 4. The paper could be read independently from the rest of this thesis. The paper presents the design of the compliant hinge, having a performance of at least a factor 30 higher compared to the best performing conventional compliant hinge. Additional information that supports the paper could be found in the appendices. Appendix A elaborates the experimental test setup. The measurement results of different experiments are shown in Appendix B. In Appendix C some design specification of the hinge and the conventional compliant hinges are presented. Appendix D provides datasheets which elaborate to the content of the thesis. Chapter 5 contains a discussion on the results of the research presented in the paper and some additional results provided by the appendices. Finally, the main conclusions are drawn from the results of the paper and the appendices. The conclusions, together with some recommendations for further research, are presented in Chapter 6.

<div style="text-align: right; font-size: 4em;">2</div>

Fundamentals of a closed fluid pressure balancing hinge

The proposed compliant hinge consists of a single standard element, closed form pressure balancing. The cross section of the most basic embodiment of the compliant hinge can be seen in Figure 2.1. The Figure on the left shows the complaint hinge while actuated by a normal displacement and the Figure on the right shows the compliant hinge while the actuated by an angular displacement, both displacement are applied on the bottom surface of the compliant hinge. The actuated displacement is proportional to the height of the hinge. The fluid is enclosed and kept in place by the deforming material during deformation of the hinge. Subsequently the applied force is diffused by the fluid on the inner surface of the proposed hinge, causing stress on the boundary material. In this thesis all finite element analysis (FEA) are performed by *COMSOL*, and *Matlab* is used for all mathematics [22, 23].
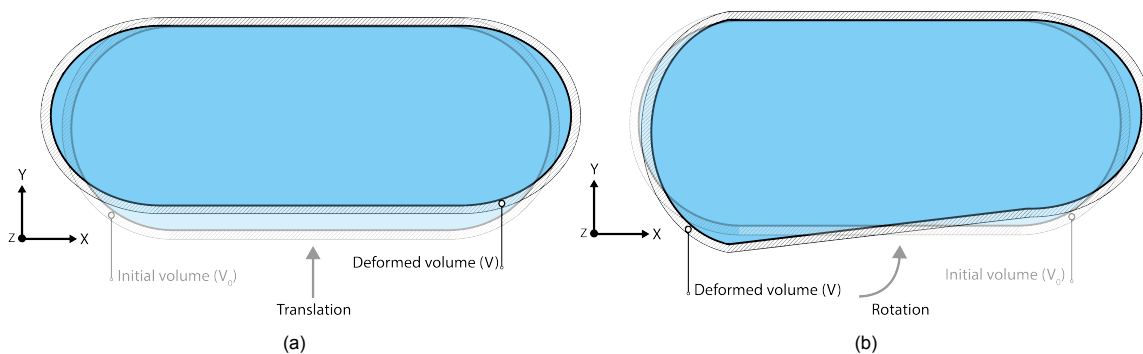
Figure 2.1: Schematic overview of the 2D hinge design for its initial volume and deformed volumes actuated by a prescribed normal displacement (a) and prescribed angular displacement (b).

In the course of this Chapter the various components, the corresponding working principles and boundaries of the proposed compliant hinge are elaborated.

2.1. Geometric shape

To obtain insight in the behaviour of this type of hinge, a 2D hinge design is made. The basic embodiment of the hinge consists of three geometric parameters: *l, h, t*. The 2D shape of the compliant hinge is constructed by these three parameters to acquire an elementary design, see Figure 2.2. The

<div style="text-align: center;">3</div>

elementary design could learn us more about the fundamental behaviour of such enclosed fluid cell while actuated by various deformations.

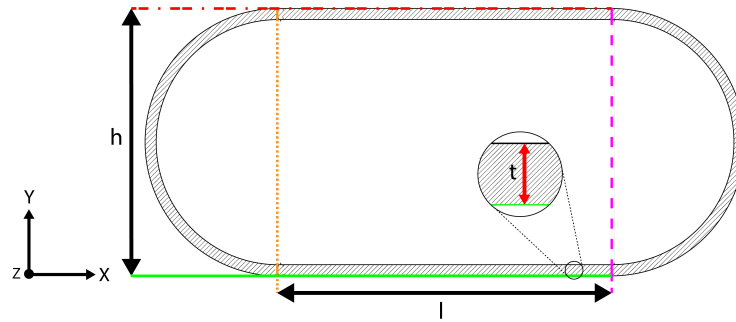Figure 2.2: Schematic overview of 2D hinge design for which the geometric parameters *l, h, t* are indicated by different colours and lines. *l* is the distance between the left edge (dot) and right edge (dash) of the parallel walls. *h* is the distance between the upper (dash-dash-dot) and lower (line) edge of the parallel walls, and *t* is the dimension across the width of the wall.

The Figure shows that the hinge is enclosed by a boundary material with a thickness *t*. The middle part of the hinge consist of two parallel beams, the outside surfaces of these parallel beams is parted by the height *h*. The sides of the hinge consists of material curves, connecting both the parallel beams to each other. These so-called 'side curves' are designed as a semicircle with radius $\frac{h}{2}$. For a larger radius, the side curves will increase in surface, enlarging the absolute length of the hinge. However, the length parameter *l* does not include the constitution of these material curves and defines only the length along the parallel walls in the middle of the compliant hinge. The additional length of the side curves is not included in the length parameter of the compliant hinge because the first examinations on the hinge showed that a relatively large length *l* and relatively small height *h* obtain desired measurement results, causing the additional length of the curves to be relative small compared to the length of the parallel beams.

A varying boundary thickness *t* will differ the behaviour of the hinge and introduce an additional variable to the calculations on the hinge [19]. Therefore we assume a constant magnitude for the initial thickness *t* along the entire geometry. For the design of the hinge, the material thickness *t* induces an inner- and outer-boundary. The inner boundary is holding the fluid inside the hinge while the outer boundary is connected to the surroundings of the hinge.

2.1.1. Constant volume

As mentioned before, the fluid chamber within the compliant hinge is enclosed. We assume that inside the enclosed material an incompressible fluid is located. Subsequently, we assume that the inner volume should remain constant throughout deformation, a decrease in volume could dissipate the actuated force on the hinge, causing a decrease in performance. During deformation the volume of the hinge tends to decrease, because of the applied force on the compliant hinge. The decrease in volume causes the pressure inside the hinge to increase. To compensate this volume decrease during deformation, the boundary material of the hinge will elongate. This elongation causes the radius of the side curves to increase, compensating the decrease of the volume inside the hinge. The compensation of volume inside the compliant hinge is continuously regulated, causing the volume of the hinge to remain constant when applying the following equation,

$$(\frac{V}{V_0}) - 1 = 0 \tag{2.1}$$

Where V_0 represents the initial volume of the compliant hinge over the inner boundary. The magnitude of the deformed volume V should remain equal to the magnitude of V_0 for the assumption of constant volume. To calculate the deformed volume (V) we will use a powerful tool of integral calculus, called, '*the theorem of divergence, or the theorem of Gauss*' [24]. Gauss's theorem states that a closed surface is equal to the volume integral of the divergence over the region inside the surface, Gauss equation is denoted as,

$$\iiint_V (\nabla \cdot \vec{F}) dV = \oiint_S (\vec{F} \cdot \vec{n}) dS \tag{2.2}$$

For this equation $\vec{F}$ represents the vector field of the deformed surface and $\vec{n}$ denotes the normal vector on the inner surface of the boundary material. The vector field of the deformed boundary material is obtained for the global coordinates system. The displacement of each material point is expressed by a material vector $\vec{F}$. The material vector field $\vec{F}$ is divided in components *x,y* and *z*. Each component represents a scalar part of the field vector. Similar, normal vector $\vec{n}$ is divided in components n_x, n_y and n_z. Since the volume of the inner boundary is calculated the normal vectors point 'inwards'. The schematic representation of the normal vectors is shown in Figure 2.3.
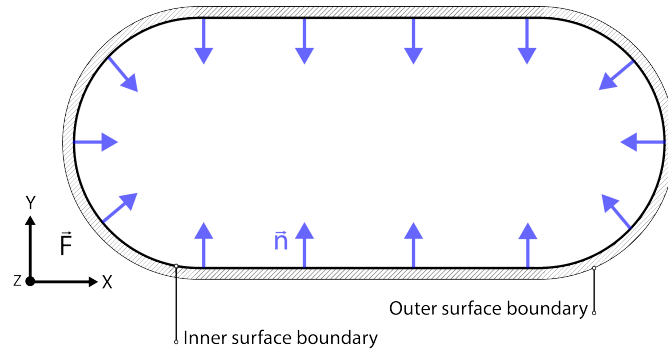

Figure 2.3: Schematic overview of 2D hinge design, static vector field $\vec{F}$ of the material and normal vectors $\vec{n}$ located at the inner boundary of the compliant hinge.

To obtain the volume of the examined surface, the left part of equation 2.2 should only contain the parameter of the deformed volume. In order to exclude the deformed volume, the divergence of the vector field should equal the following,

$$(\nabla \cdot \vec{F}) = 1 \tag{2.3}$$

The divergence ∇ of the vector field $\vec{F}$ should equal one. For a value of one, only the integral of the deformed volume will remain on the left side of the equation. This means that the right sided equation equals the deformed volume of the deformed hinge. The vector field corresponding to the displacement of each material point is expressed as,

$$\vec{F}(x, y, z) = \frac{1}{3}(x, y, z) \tag{2.4}$$

Since we observed that the ∇ of $\vec{F}$ should equal one, the ∇ of the individual x, y and z components equals $\frac{1}{3}$. During deformation of the hinge the initial shape will change. This change induces an deformation of the side curves, resulting in a positive divergence. If we use Gauss's theorem for the applied conditions, we find the following equation for the deformed volume of the hinge,

$$V = -\int \frac{(n_x \cdot x + n_y \cdot y + n_z \cdot z)}{3} \tag{2.5}$$

The opposite direction of the vector field $\vec{F}$ and the normal vectors $\vec{n}$ cause a negative value for the dot product of these vectors. To eliminate this negative result a minus is placed in front of the equation.

The initial pressure *P* inside the hinge is by definition not equal to the atmospheric pressure. The pressure inside the hinge is determined by the water inside the hinge, as the pressure inside the hinge increases on deformation. However, the pressure inside the hinge could also be defined by the temperature or amount of water inside the compliant hinge. For various actuated forces the deformation of the hinge induces a specific stiffness along its length *l*.

The design of the proposed hinge is elementary, as it consists only of three geometric parameters. For this elementary design we assume that the deformation of the compliant hinge is only dependent on the deformation of the side curves, as the parallel middle beams are selected rigid. If we look further

at the elementary design of the proposed hinge we find that the unit of the normal stiffness is $[N/m]$, while the unit for the rotation stiffness is $[N \cdot m]$. The difference of these units is schematically induced by the relationship of the Young's modulus E to the geometric thickness t of the boundary material. The development of the normal stiffness is linear $(E \cdot t)$ while the development of the rotation stiffness is non-linear $(E \cdot t^3)$. These function are derived from the equation of the Hoop stress [25].

2.2. Model stiffness

The stiffness model of the compliant hinge constitutes the basis of modelling the performance. The stiffness is defined by three different deformations: compression, rotation and lateral shear. The lateral deformation of the hinge is not considered in this study, since the stiffness is predominantly defined by shear stiffness of the front and back plane of the hinge, as a result, substantively higher than the rotation stiffness, which is the results of the bending stiffness of the outer shell of the hinge. Moreover, we are only interested in the stiffness introduced by the compression and rotation of the compliant hinge. The normal stiffness is calculated by the integral of the traction $\vec{F}$ for a normal displacement on the hinge. The rotation stiffness is calculated using the integral of the traction $(M = F \cdot l)$ multiplied by the arm, defined by the geometric length l. The force $\vec{F}$ is obtained by the surface integral over the traction for the actuated surface of the hinge $[N/m^2]$ [26], shown in the following equation,

$$\vec{F} = \int \vec{T} dA = \int (\vec{\sigma} \cdot \vec{n}) dS \tag{2.6}$$

The equation shows two different options to calculate the reaction force $\vec{F}$ in Newton $[N]$. Both options show that the force is determined by the integral over the actuated surface. The traction forces are calculated by the Cauchy stress tensor for the deformed state of the material [27], and are calculated by the following equation,

$$\boldsymbol{T} = \vec{\boldsymbol{\sigma}} \cdot \boldsymbol{n} \tag{2.7}$$

Here, $\vec{n}$ represents the normal vector on the actuated surface and $\vec{\sigma}$ states the stress matrix on the actuated boundary material. For the 2D model, the stress matrix consists of four elements and two vectors in the x and Y direction. Where for the 3D model, the stress matrix consists of nine elements and the three vectors in the X, Y and Z direction. For the stress matrix the magnitudes of the opposing shear stresses are always equal due to symmetry, which is common in all equations involving stress and strain. The uni-axial stress is determined by $\vec{\sigma}$ and the shear stress is determined by $\vec{\tau}$. The traction T is indicated on the left side of both equations. A schematic representation of the traction is displayed in Figure 2.4.
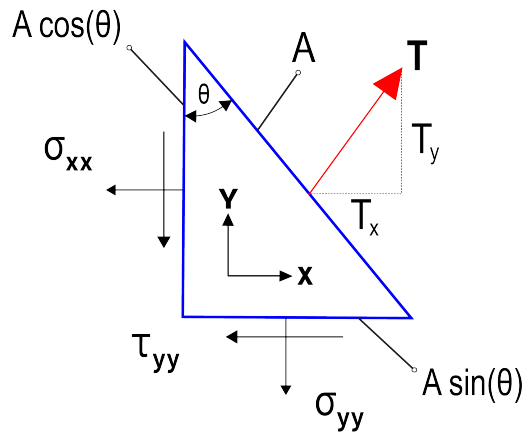

Figure 2.4: Schematic overview of a material cross section and the parameters used to determine the traction $\vec{T}$ on the cross section.

The traction force is determined over the actuated surface of the compliant hinge. In particular, over the same surface as the prescribed displacement is actuated.

2.2.1. Normal- or support-stiffness

The prescribed displacement δ is applied perpendicular to the rigid bottom surface of the hinge (positive Y-axis), see Figure 2.1a. The displacement is applied relative to the height h of the hinge and could be defined using the following equation,

$$\delta = \lambda_f h \tag{2.8}$$

Here, h is the geometric height parameter. The prescribed displacement is denoted as a percentage of the height h and is described by λ_f. For the parameter sensitivity analysis and parameter sweep λ_f is set to 1%, as the material is assumed linear elastic. For the other measurement done in this thesis λ_f is set to 6.25%. For the normal displacement the fluid inside the hinge diffuses the actuated force identical over the side curves and corners. The side curves deform identical, applying the force of the deformation along a relative large surface (Appendix B.2). If we look in literature, the stress on the boundary material for the normal displacement could be partially indicated by the Hoop stress [25], as only the side curves deform on deformation of the compliant hinge. Subsequently, the Hoop stress could be used to calculate the deformation and the load capacity of the material for normal displacement on the hinge.

2.2.2. Rotation stiffness

In order to compare the normal- and rotation-stiffness, both prescribed displacements should equal magnitudes. The rotational displacement is defined by the arc length of the bottom surface edge, perpendicular to the rotational axis (Z-axis), shown in Figure 2.1b. The edge displacement is equal to,

$$\delta = \frac{l}{2}\theta \tag{2.9}$$

The angle of rotation θ is applied on the centre line of the actuated surface. The rotation stiffness is induced by a mechanical moment on the compliant hinge. This moment is applied on the edge of the actuated surface, which is indicated by the length l of the compliant hinge. The angle of rotation is defined by the following equation,

$$\theta = \frac{h \cdot 2\lambda_f}{l} \tag{2.10}$$

The prescribed rotation (θ) is dependent on the variation in height h and length l, since the edge displacement of the bottom surface is dependent on a change in angle. The applied force compresses the actuated surface of the hinge, introducing a decrease in angle of rotation. The compression of the applied force is not measurable on the demonstrator. Therefore, the rotation stiffness of the 3D FEM model and demonstrator are calculated by the recalculated angle of rotation obtained by the 3D FEM model, for prescribed displacement of 6.25% of the height h.

When the rotation is applied, the total hinge deforms. The deformation causes one side of the hinge to compress and the other side to expand. This deformation causes a shift of the volume inside the hinge. Since the volume remains nearly constant, the volume shift induces a small elongation stiffness upon rotation. Therefore, the rotation stiffness of the hinge is largely determined by the structural stiffness of the hinge. The stress in the boundary material could not solely be defined by the Hoop stress. The stress in the boundary material upon rotation is mostly caused by the volume enlargement of the spherical corners and cylindrical side curves of the boundary material, along with an elongation of the boundary material.

2.2.3. Performance

The proposed hinge to the conventional compliant hinges by the normal- and rotation-stiffness. The resulting hinge should desirably have a high normal-to-rotation stiffness ratio, in this work defined as performance, to exceed the conventional stiffness ratio of compliant hinges. To increase the range of operation the rotation stiffness of the compliant hinge needs to be reduced while maintaining the normal- or support-stiffness. To obtain such high performance, a low bending stiffness and high hoop stiffness are required. Particularly the thickness parameter t greatly effects the general behaviour of the

hinge. The performance is defined as a function of the normal- and rotational-stiffness and is defined as follows,

$$\lambda_r[\theta/m^2] = \frac{K_n[N/m]}{K_r[N \cdot m/\theta]} \tag{2.11}$$

Here K_n is the normal stiffness and K_r the rotation stiffness. The ratio for the normal- and rotation-stiffness is denoted as λ_r. The unit of K_n is $[N/m]$ and the unit for K_r is $[\theta/m^2]$. Showing that the performance is not dimensionless. The objective of the project is to design a compliant hinge that has a relative large normal stiffness and relative low rotation stiffness. Whereas the performance of the proposed hinge is compared to the performance of conventional compliant compliant hinges [28]. The stiffness magnitudes of these conventional compliant hinges are shown in the Appendix C.2.

What could be observed, from the Table in Appendix C.2, is that a trade-off is made between high normal- or support-stiffness K_n and a high stiffness ratio. And even then, the ratio is limited to an order of $\lambda_r = 500$. The behaviour of these conventional compliant hinges could be compared to the behaviour of the proposed hinge as the actuated motion is similar [28]. The shapes of the selected conventional compliant hinges are different by design. However, the geometric dimensions of the selected conventional compliant hinges could be fitted in a design space of a cube consisting equal edges of $2.5E^{-2}m$. For that case we assume that the design space of the selected conventional compliant hinges is a cube with equal edges of $2.5E^{-2}m$.

2.3. Material properties

The fluid inside the hinge is secluded by a boundary material. In order to manufacture this boundary edge, a castable silicone material is selected [29]. Since we are not able to construct the total hinge in one run, we assume that the bonding region of silicone to silicone possesses similar material properties as the silicone material [30]. To form the silicone material, the silicone is added to a hardener, for a mutual weight ratio of one. The used silicone has a shore hardness of A40. To determine the material properties, for implementation in FEM, an ISO:37 [31] tensile strength test is performed.
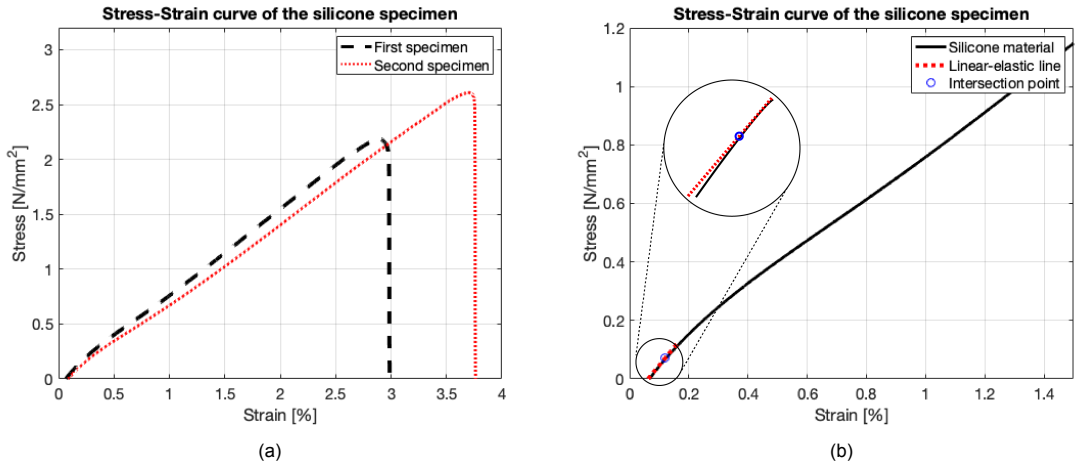

(a)

(b)

Figure 2.5: Plots of the stress-strain curves for the tested specimen. (a) Stress-strain curve of the silicone material for both specimen. The difference is strain is caused by an instant release of the specimen from the clamp of the testing machine. (b) Stress-strain curve of the average value for the stress-strain curves of both specimen. The region of interest is the slope for small deformations (1% Strain). The window shows an zoomed view of the tangent linear-elastic line.

Figure 2.5a shows the stress-strain curves of the two specimen tested for the silicone material. The measurement results have a variation of approximately $10 - 15\%$ along the plots of both specimen. The measurements on both specimens were instantly released from the clamp of the machine during the test. The instant release was a consequence of a decrease in material thickness by the elongation of the specimen. The clamps were not actively compressing throughout the measurement on the attachment points of the specimen. This resulted in a decrease of grip on the specimens, instantly releasing the contact with one end of the specimen. The two specimen released itself at a different elongation length, causing the strain (%) of both measurement to have a different magnitude.

Both tested specimens are manufactured by the same run of hardened silicone, most likely having the same material properties. The tested specimens and the demonstrator of the compliant hinge are produced for different runs, hereby the mutual material properties can variate. For the tensile measurements results of both specimen we take the average of the traction force and use that as the benchmark for the material properties. Here a range of 15% for the Young's modulus is set up around the benchmark of the material properties: $1.2 \pm 0.18 MPa$ [32]. The selected Young's modulus for the detailed 3D FEM model is $1.061 MPa$, while we assume a Poisson ratio of 0.49 for the hyperelastic silicone [33, 34].

After the individual measurements on both specimens, the specimens were both actuated till failure. The failure measurements are not included in this thesis, since the properties of the material were changed by to the first measurements. These raw data of these first measurements is shown in appendix B.1.

Figure 2.5b shows the average stress-strain curves of both silicone specimen. In this thesis the compliant hinge state a maximum deformation of 6.25% of the height. To simplify the calculations, the Young's modulus E is defined for a linear elastic material model at 1% of the strain. To determine the stiffness of the stress-strain curve, we could use the tangent- or secant-stiffness. The secant stiffness calculates the average rate of change over the whole concave curve [35]. However, we want to determine the Young's modulus at this exact point of the stress-strain curve, thus the tangent stiffness is selected.

From the stress-strain curves we could see that the elongation stiffness of the silicone along the length of the silicone material is relative large. Literature shows that the bending stiffness of the silicone material is relative low compared to the elongation stiffness [36].

2.4. Fluid properties

The fluid inside the hinge is of great importance for the overall behaviour of the hinge. The prescribed displacement on the hinge induces a force which is diffused by the fluid over the inner surface of the hinge. It is important that the fluid inside the hinge is incompressible, otherwise the fluid will dissipate the energy of the deformation. Therefore a gas could not be used, as the compressibility of gasses is too high [37]. Also a solid could not be used, as a solid contains shear stress on deformation [38]. We want to avoid shear stress as presence of shear stress increases the rotation stiffness of the compliant hinge.

To simplify the realization of the hinge, tap water is chosen as fluid inside the hinge (Appendix D.2). The properties of tap water tend towards incompressibility and therefore corresponds to the demands of the fluid inside the hinge. To define the properties of the water we take a look at three quantities: Poisson ratio, Shear stress and Bulk modulus.
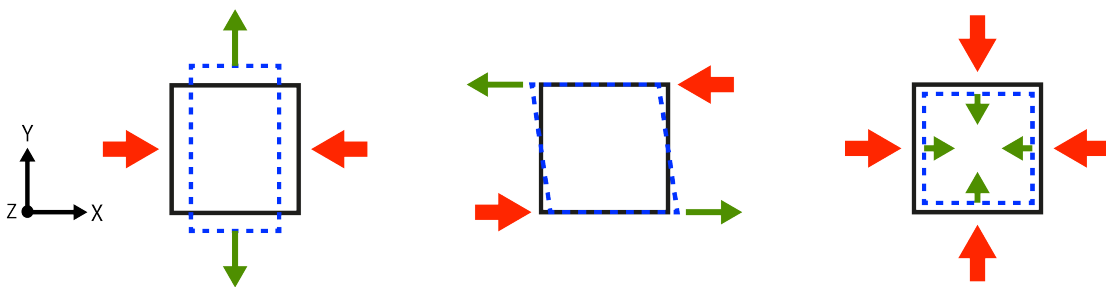
Figure 2.6: A schematic overview of a square shaped material examined for the Poisson ratio, shear- and bulk-modulus, respectively. The big (red) arrows represent the direction of stress exerted, the small (green) green arrows represent the axis along which the response is measured.

The Poisson ratio is divided by the relative contraction strain normal to the applied load (ϵ_y) and the relative extension strain perpendicular to the applied load ϵ_x. The Poisson Ratio could be expressed as,

$$\nu = -\frac{\epsilon_x}{\epsilon_y} \tag{2.12}$$

A schematic overview of the Poisson ratio on a piece of material is shown in Figure 2.6. The Poisson ratio of an incompressible fluid is assumed to be 0.5 [39].

The shear stress $[N/m^2]$ represents the component of stress co-planar to the material cross section. Apply a shear stress to a liquid and it continues to deform at a constant rate until the stress is removed, hereby the deformation Δx will tend to infinite [38]. Therefore, the shear modulus of an ideal liquid is assumed to be zero [40]. The equation to calculate the shear stress is the following,

$$G = \frac{\tau_{xy}}{\gamma_{xy}} = \frac{Fl}{A\Delta x} \tag{2.13}$$

Here, G is the shear modulus or modulus of rigidity, τ_{xy} is the shear stress and γ_{xy} is the shear strain. A schematic overview of the shear modulus on a piece of material could be seen in Figure 2.6.

The bulk modulus measures the decrease in volume for an increase in pressure. The 'modulus of elasticity' of a liquid varies widely, depending on the specific gravity and temperature of the liquid. The bulk modulus is calculated by the following equation,

$$K = -V\frac{dP}{DV} \tag{2.14}$$

Where P is the pressure, V is the volume and $\frac{dP}{dV}$ denotes the derivative of pressure with respect to volume. As mentioned before, the water inside the compliant hinge is approximately incompressible. This could also be observed by the Bulk modulus for water which is relatively high, $2.2E^9 Pa$. A schematic overview of the bulk modulus on a piece of material could be seen in Figure 2.6.
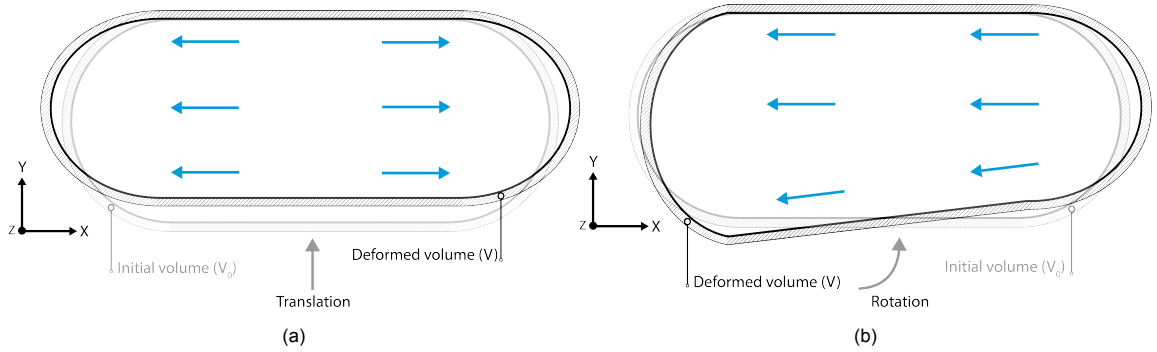

Figure 2.7: Schematic overview of the 2D hinge design for its initial volume and deformed volumes actuated by a prescribed normal displacement (a) and prescribed angular displacement (b). For both deformations the assumed fluid distribution inside the hinged is visualized.

The assumed fluid distribution inside the hinge gives an schematic overview of the assumption made for the normal- and rotation-stiffness on the proposed hinge. During the normal deformation the fluid inside the hinge diffuses proportionally towards the side curves. The normal deformation is mostly determined by the elongation of the silicone material. For rotational deformation the fluid inside the hinge shifts to the expanded side of the hinge, since one side of the hinge is compressed. The rotational deformations is mostly determined by the bending of the silicone material. As a results, we state that the relative large normal stiffness and relative low rotation stiffness of the hinge are caused by the fluid properties of the water.

The initial volume of hinge is used to fill the inside of the hinge for a certain volume of water, as it is difficult to indicate if the hinge is totally filled with water. The design of 3D hinge consists of an initial volume of $7.7813E^{-6}m^3$ for the first configuration, which is equal to $7.78mL$. Since the density of water is $997\frac{kg}{m^3}$ the mass of the water inside the hinge is shown by the following equation [41],

$$997\frac{kg}{m^3} \cdot 7.7813E^{-6}m^3 = 7.76 \cdot 10^{-3}Kg \tag{2.15}$$

3

Hinge design

Now we obtained the fundamental working principle of the closed form pressure balanced hinge, we could construct the demonstrator. This Chapter elaborates the chosen geometric parameters and discusses important design aspects that have to be taken into consideration to manufacture the demonstrator.

3.1. Parameter sensitivity analysis

First, a 2D parameter sensitivity analysis is performed to observe the behaviour of the individual parameters. The development of the stiffness is of interest during this parameter sensitivity analysis. Various exploratory simulations on the convergence and stability of the solutions showed us that a hinge shape for a larger length than height provides desired results. The exploratory research on the shape of the hinge showed that the most converging solutions are obtained for a $\frac{l}{h} > 1$, therefore the lower boundary is set to one,

- $1 \leq \frac{l}{h} \leq 100$

- $1 \leq \frac{h}{t} \leq 100$

The range of variation was selected to cover two orders of magnitude for the individual parameter variation. Within these ranges we found that multiple configurations introduce non-feasible deformations. For internal collisions of the boundary material to its own structure a lower boundary is set for the non-converging simulations. A schematic overview of the collision on the inside of the hinge is shown in Figure 3.1.

In this Figure the ratio between the height h and the thickness t of the compliant hinge is too small to apply the desired deformation, as the inner boundary collides to the opposite inner boundary of the hinge. This collision induces divergence for the solutions of the simulation. The lower boundary for $\frac{h}{t}$ is set on 4, below this geometric ratio the solutions of the hinge are not feasible for every deformation. The lower boundary of ratio $\frac{l}{h}$ is set on 2.5, since all the simulations converge from this geometric ratio. For extremely small deformations the stiffness magnitudes of the traction force occasionally become negative, as the non-converging solution is too soon within the FEM tolerance. This could be prevented by enlarging the compliant hinge. The negative traction force occurs more often when the consecutive ratio of the of the boundary $\frac{l}{t}$ is approximately 40. Therefore the higher boundary of both geometric ratio's forms a multiplication of 40, as shown below,
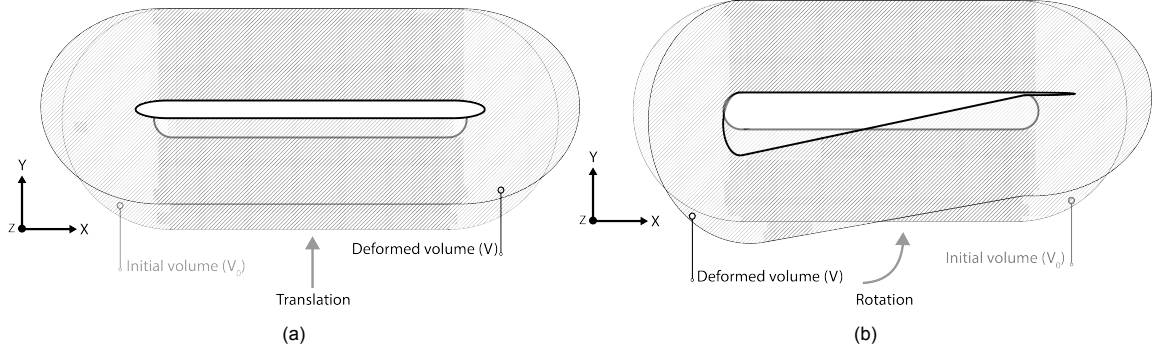
- $2.5 \leq \frac{l}{h} \leq 4$

Figure 3.1: Schematic overview of initial 2D hinge volume and the 2D hinge deformed volume for a prescribed normal displacement (a) and prescribed angular displacement (b). Here $\frac{h}{t}$ is approximately 3, causing the applied prescribed rotation to introduce internal collision of the boundary material.

$$\bullet \; 4 \leq \frac{h}{t} \leq 10$$

This new range causes stable converging solutions for all measurements done in FEM. The chosen range for the length l is within the boundary range of the conventional compliant hinges, as we set the range of the length to, $10mm - 25mm$. Consecutively the ranges of the height, $6.25mm - 10mm$ and the thickness $1mm - 2.5mm$ are determined by the selected parameter ratios. The linear elastic material, used in these simulations, is characterized by an linear relation between stress and strain [42], shown in the following equation,

$$\vec{\sigma} = E \cdot \vec{\epsilon} \tag{3.1}$$

The individual parameter variation does not depend on the material properties (E, ν, ρ), making the exact stiffness magnitudes on the parameter sensitivity analysis irrelevant. Instead, the values on the y-axis of the parameter sensitivity analysis show the relative change in stiffness magnitude over the variation of the various parameters. In these plots the initial 2D hinge design is indicated by a circle to act as reference for the variation in stiffness.

3.2. Global parameter sweep

Now the behaviour of each individual parameters is known, a case study is used to analyse the performance of the detailed hinge. A global parameter sweep is performed to indicate the geometric parameter values corresponding to the highest performance within the given 2D boundary design. To ensure a fair comparison between the compliant hinge an the state of the art compliant hinges, the normal- and rotation-stiffness should be related to the conventional stiffness magnitudes (Appendix C.2) based on the following statements,

$$\bullet \; 100 \text{ [N/m]} < K_n \text{ of the proposed hinge}$$

$$\bullet \; 10 \text{ [N·m/}\theta\text{]} > K_r \text{ of the proposed hinge}$$

The stiffness magnitudes are presented based on the average magnitudes of the normal- and rotation-stiffness of the conventional compliant hinges, shown in Appendix C.2. The average of these conventional magnitudes are $49.50 N/m$ and $5.85 N \cdot m/\theta$, respectively. The stiffness values are respectively rounded to create a desired boundary for the normal- and rotation-stiffness of the proposed hinge. The boundaries prevent the hinge from large overall stiffness. Since a large overall stiffness could cause malfunctions for the implementation in current compliant hinge applications, as the hinge not provides a rotation stiffness low enough to obtain the desired angle of rotation for the same input force.

For all simulations done in this thesis the FEM makes use of a non-linear solver. The non-linear solver is used to coop with the non-linear deformations of the silicone material [43, 44]. The non-linearity could be visualised by the Green-Lagrange equation for normal strain [24]. The quadratic

term(s), depending on 2D or 3D, at the end of the Green-Lagrange equation implies the non-linear deformations induced by the silicone material.

In a geometrically linear setting, the equations of equilibrium are formulated in the undeformed state and are not updated with the deformation. For the most engineering problems this is not a problem, since the deformations are so small that the deviation from the original geometry is not perceptible. This is why a majority of analyses are made with an assumption of geometric linearity [45]. To calculate the volume of the compliant hinge continuously, the FEM makes use of geometric non-linearity, as for every step the volume of the compliant hinge should be constant. For geometric non-linearity the equations of equilibrium are formulated in the undeformed state and are updated with each deformation [46]. The displacement of the material could be calculated by the following equation,

$$\vec{x} = \vec{X}(\mathbf{x}, t) + \vec{u}(\mathbf{x}, t) \tag{3.2}$$

Here the spatial coordinates of a certain point *x* differ from the material coordinates of the same point *X* by the the displacement vector *u*. The material coordinates and the displacement vector are a function of the spatial coordinate system.

During deformation a residual force could introduces an unbalanced force for the applied load. For the non-linear FEM solver, the solver will often introduce damping [47]. The FEM damping factor in this thesis is set to one, inducing no residual forces. The used constant Newton scheme instead will cause the solver to make larger updates, having a higher computational power. The solver used in this thesis is the MUMPS solver in COMSOL [22].

3.3. Transition from 2D to 3D

We obtained a sufficient 2D geometry of the proposed hinge, now the transition to the 3D model is needed. A choice with respect to the revolved design is made. The choice is based on a large normal stiffness and a low rotation stiffness for the 3D design of the compliant hinge.
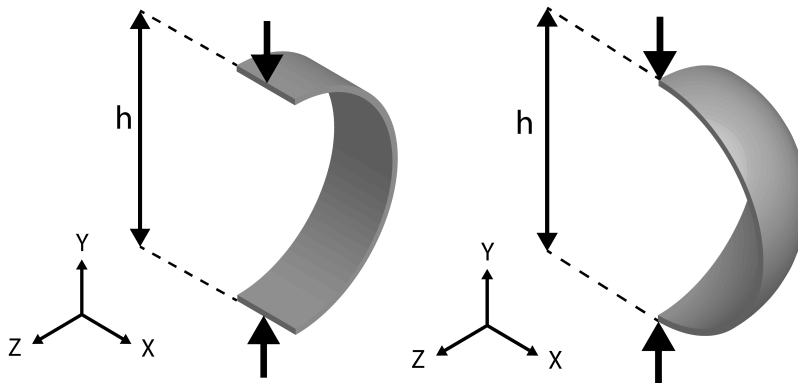

Figure 3.2: Schematic overviews of a 3D half cylinder shape and a 3D quarter sphere shape. (a) An overview of a half cylinder for an axial applied load. The half cylinder represents a side curve of the proposed hinge. (b) An overview of a quarter sphere for an axial applied load. The quarter sphere represents a corner of the proposed hinge. The arrow represent the applied force on the different shapes. The Figures are solely used to visualize the axial force on the shapes.

To obtain the 3D design of the hinge we needed to perform a transition from the 2D hinge design to the 3D hinge design. For the transition we did not revolved the 2D design around its middle point, as a revolved 2D design would cause a round shaped 3D model for which the sides around the design are basically spherical corners. The disadvantage of a spherical shape is that the axial stiffness is higher than the axial stiffness of half a cylinder, visualized in Figure 3.2 [48]. Therefore, a round shaped 3D hinge design will induce a relative higher bending stiffness than a square shaped 3D design. This high structural stiffness causes the rotation stiffness to be undesired high during deformation, decreasing the performance of the compliant hinge. The transition is performed by adding a depth parameter *d* to the 2D hinge design, here the 2D geometry of the compliant hinge remains while adding a third dimension. The scaling in depth *d* is used to calculate the traction force for a selected depth of the

2D hinge design. This helps us to compare the traction forces on the 2D FEM model and the 3D FEM model.

To obtain a design that is stiff for a normal displacement and compliant for an angular displacement. The fluid inside the hinge should induce high normal stiffness, as the structural design should be relative compliant. Otherwise the rotation stiffness will become large, as it is mostly depends on the bending stiffness of the hinge. We assume that the 2D hinge design is enclosed by two vertical plates on the visual front and back. The axial stiffness induces by a vertical plate is high. For the 3D model of the compliant hinge, the side curves of the 2D hinge model are places on either side of the hinge and the corners are designed as quarter spheres. Each corner sphere is connected to two side curves around the proposed hinge.

3.4. Detailed design

The detailed 3D analysis of the hinge is obtained to determine a more accurate performance of the proposed hinge. The parameter sweep provides us two different 2D hinge configurations for the demonstrator. The traction force on these configurations is measured by a Zwick-Roell Z005 (Appendix D.3), which uses compression to apply the prescribed displacement to the surface of the hinge.

The feasible boundary domain of the demonstrator has chosen to be exactly a factor two larger than the boundary domain of the conventional hinges. This is done to overcome the small non-feasible size of the proposed hinge. The small sized hinge induces a smaller mesh size for the FEM model, this smaller model needs more computational power to solve the model. The extended computation power and the boundary domain of the feasible design constitute to the design space of the demonstrator. The measured stiffness magnitudes on the demonstrator are compared to the stiffness magnitudes of the selected conventional compliant hinges. In general hinges are constrained to have one axis of rotation, however the proposed hinge is able to rotate around multiple axis. Therefore the proposed hinge could be seen as a joint. The rotation stiffness around the X and Z-axis are similar (Figure 3.4a, as the dimensions of the proposed hinge are perfect symmetric. To constrain the proposed joint to one axis of rotation, the surface of the proposed hinge could be connected to the surface of another proposed hinge. The combination of these hinges induces a series that will only rotate around one selected axis. Another solution would be to redesign the geometry of the compliant hinge to obtain rotation around only one axis.

The rotation of the proposed hinge should be aligned along the shortest distance across the hinge. This means that the proposed hinge is rotated along its length l around the X- or Z-axis, shown in Figure 3.3. A larger distance to the middle of the hinge would induce a larger mechanical moment and thus a larger rotation stiffness.

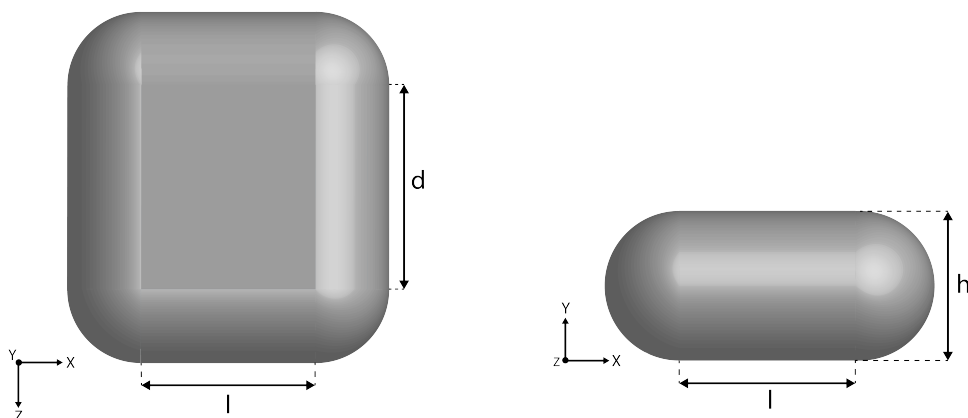Figure 3.3: Schematic overviews of 3D hinge design. (a) The top view of the 3D hinge design. (b) The side view of the 3D hinge design. The indicated dimension are corresponding to the detailed hinge design.

We assume that a larger design induces larger displacements and larger forces. An incidental benefit of the demonstrator are the relative large traction forces which do not tend towards wrong

solutions, for which diverging solutions of the simulation are within the tolerance of the FEM solver. The larger displacement is also convenient to fit the range of the testing machine.

For a displacement of 6.25% of the height *h* we obtained an angle of rotation equal to $2.86°$ ($0.05 rad$). The magnitude of this angle does not corresponds to the angle of rotation made by the conventional compliant hinges, seen in Appendix C.2. The maximum angle of displacement for the proposed hinge is located around $45°$, tested by hand. For this angle of rotation the inner boundary of the demonstrator of the second configuration collides to its own structure, as shown in Figure 3.1. The maximum angle of rotation for the first configuration is slightly smaller.

The load capacity is the maximal demanded stress that the material of the hinge could withstand without failure and is not equal to the stiffness magnitudes of the hinge. To examine the maximal loads on the proposed hinge we looked at the strain energy density $[J/m^3]$ and the shear stress $[N/m^2]$ in the material [49]. During deformation we came to the conclusion that the maximal FEM deformation of 6.25% causes the magnitudes of the shear stress and the strain energy density to increase constantly. If the material boundary of the compliant hinge would fail for this deformation, we would expect a large increase for one of these quantities, however the stepsize remains similar towards the maximum displacement in FEM. We suggest that the FEM model is not sufficient to calculate the maximum displacement of the model as it is limited by unproportionally large deforming elements. Therefore we could not examine the load capacity of the proposed hinge.

The deforming compliant hinge for the normal- and rotation-displacement in COMSOL is shown in Appendix C.1. When applying the normal- and rotation-displacement on the compliant hinge, the side curves and corner spheres are the only parts to deform. The large deforming surface could provide a larger displacement without reaching critical material stress, in comparison to point deformations [13]. The deformation of the compliant is visualized by the Von Mises stress on the surface of the hinge [5]. We see that the overall deformation of the compliant hinge, for a normal displacement, causes the Von Mises stress on the surface of the side curves to be relative high to the Von Mises stress on the surface of the corners, which is relative low. For the prescribed rotation the Von Mises stress is evenly distributed across the entire surface of the compliant hinge. The distribution is caused by a shift of volume inside the hinge as mentioned in Chapter 2.

3.4.1. Demonstrator

To validate the proof of concept a demonstrator is manufactured. The demonstrator is similar to the 3D detailed model of the compliant hinge. The traction force of the demonstrator is measured by a test machine (Appendix D.3). The joint connector simulates the rigid surface of the proposed hinge while making contact to the testing machine. To verify the rigidness of the joint connector an aluminium plate is used. Both configurations are elaborated in this section.
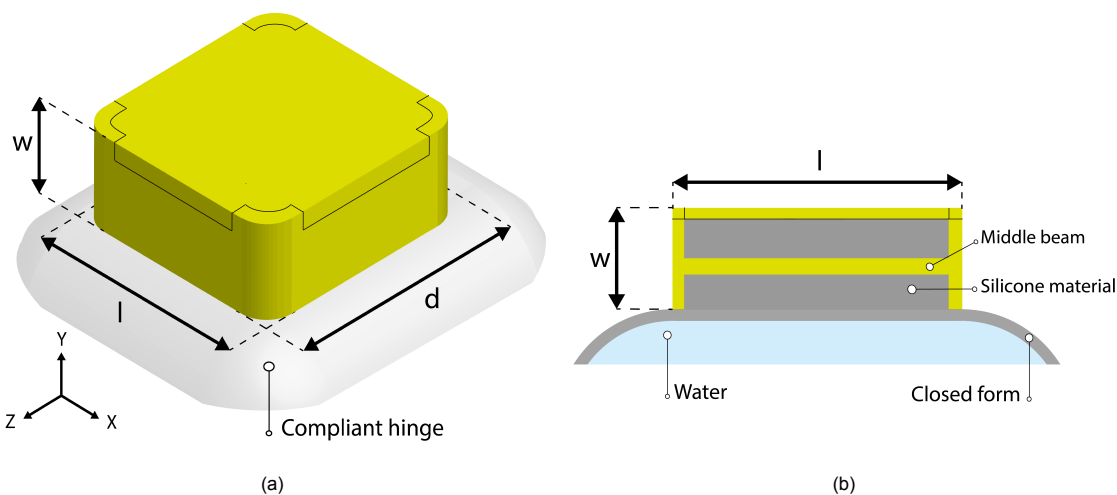
Figure 3.4: Schematic overview of the joint connector. (a) Schematic isometric view of the joint connector attached to the compliant hinge. The geometric parameters l, d are corresponding to the parameters of the compliant hinge. The height of the joint connector is denoted by w and has a magnitude of $2mm$. (b) Cross section view of the joint connector, attached to the compliant hinge. The intersection is located along the middle of the depth d.

The specific joint connector is shown in Figure 3.4a. The joint connector is attached to the proposed hinge by the silicone material, enclosing the middle beam inside the structure of the joint connector, see figure 3.4b. The enclosed middle beam prevents the joint connector from separation to the hinge in the *X,Y* and *Z*-direction. The enclosed middle beam and square shape of the connector prevent the joint connector from rotation relative to the hinge in the *X,Y* and *Z*-axis, constraining the joint connector for all undesirable displacements. The top of the connector holds a lid that could be removed. The bottom holds an open surface, enclosed by the boundary material of the connector. The joint connector simulates the rigidness of the actuated surface during deformation. Visually the joint connector seems rigid. However, we do not know the rigidness of the joint connector as the inside is filled with hardened silicone. To put the joint connector to the test we compare the traction forces on the hinge obtained by the joint connector and the aluminium connector.

The aluminium connector is an aluminium plate with a thickness of $5mm$, that is connected to the compliant hinge by only friction. The aluminium plate is stiff enough to neglect deformations induced by the forces on the hinge ($< 200N$) [50]. We assume that the aluminium plate is completely rigid. In Appendix B.1 the raw measurement results of the joint connector for the normal- and rotation-displacement are shown. Also the normal displacement for the aluminium connector is shown. The rotational displacement of the aluminium connector is not shown, as the aluminium plate does not totally bond to the actuated surface of the hinge during the entire rotation. This phenomena could been seen in Appendix A.1, were the bonding between the aluminium connector and the proposed hinge induces a gap during rotation. The gap introduces an incorrect magnitude of the traction force for the rotation, as the boundary of the hinge is not deforming to the displacements of the aluminium connector.

Furthermore, the measurement results on the aluminium surface are more consistent than the measurement on the surface of 3D printed PLA, see Appendix B.3. The irregularities on the joint connector are the results of the vertical aluminium plate which slides along the top surface of the connectors when applying the angular displacement. The material to material contact causes disturbance as the surface of both materials is not completely smooth. For the measurement results we assume that the sliding aluminium to aluminium surface contact is more smooth than the sliding aluminium to 3D printed PLA surface contact [51].

3.4.2. Measurement results

The measurement results of the joint connector and the aluminium connector are shown in Appendix B. The slope of the measurement results for the normal forces on both configurations is in close correspondence. However, the normal force of the joint connector is almost constant at the first part of the graph for the first configuration. What could be seen in all measurement results, on both configurations, is that there is a preload applied to the proposed hinge. The preload is present has a magnitude of $0.4N$. On could see that the preload applied to the rotation is relative higher, since the rotational traction force is lower than the normal traction force.

The joint connector is actuated by the vertical plate to introduce angular displacement. This vertical plate applied a force on the edge of the joint connected to induce a moment on the proposed hinge. During this actuation the other side of the joint connector is also compressed towards the hinge, this causes the angle of rotation to decrease. To define the actual angle of rotation, the total compression, induces by the prescribed displacement, is determined. For the experiment test setup on the demonstrator this method is not applied, since we could not indicate the total compression of the hinge. We assumed that the compression on the demonstrator is in close correspondence to the compression of the 3D FEM model. Subsequently we calculated the rotation stiffness of both models by the revised angle of rotation. However, the total compression of the hinge due to the applied mechanical moment is low ($< 5\%$ of the height), having little influence on the rotation stiffness of the compliant hinge.

The comparable magnitude of the traction forces is located at the end of the deformation. For both configurations the measurements on the demonstrator is repeated 3 times. The measurement results of the normal force state a mutual difference of approximately 1%, based on a normal displacement of 6.25% of the height h. For the measurement results of the rotation force the tip of the top plate glides along the rough surface of the joint connector, causing irregularities in the measured data. To compensate for both prescribed displacements the three measured traction forces are curve fitted by the Matlab command '*cftool*' [23].

The load capacity and maximum angle of rotation of the hinge are not determined. As the range of operation and the corresponding stiffness values could be determined for small displacements. To show

the effect of an additional amount of water and a larger normal displacement on the compliant hinge, we added a 15% surplus volume of water inside the compliant hinge. This larger volume of water creates a larger initial pressure inside the compliant hinge. Furthermore, we tested the normal displacement on the hinge for 17.5% of the height h, causing the prescribed normal displacement on the hinge to be $3.5mm$, see Appendix B.3. The measurement results on the compliant hinge showed a steeper slope compared to the slopes on the previous shown measurement (Appendix B.1). Additionally, a non-linear part is shown for small deformations. Nevertheless, we showed that the compliant hinge is able to coop with larger displacement. We did not applied larger displacements as we did not want to break the hinge.

4

Paper: Design of a Compliant Hinge based on Closed Form Pressure Balancing

Design of a Compliant Hinge based on Closed Form Pressure Balancing

R.F.P. Gomes[†], J.P.A. Nijssen[†], R.A.J. van Ostayen[†]

[†]Department of Precision and Microsystems Engineering, Delft University of Technology, Delft, The Netherlands.

Abstract—**Compliant mechanisms consist of a monolithic body and obtain motion through elastic deformation. Multiple compliant flexure designs are known but their range of motion and load capacity are often limited. When considering rotational hinges, improving the operational range requires reducing the rotation stiffness while increasing normal stiffness. This work introduces a novel compliant hinge design with increased stiffness ratio compared to the state of the art compliant hinges. The design makes use of a so-called closed form pressure balancing principle to obtain this high ratio. This principle utilizes incompressible fluid inside a closed body. A 2D parameter sweep is performed to identify the highest performing hinge design. Subsequently, a computational 3D analysis is performed and the resulting design is realized as a demonstrator. The performance is compared to conventional compliant hinges based on the ratio of the normal- and rotation-stiffness. This showed an increase of at least a factor 30 on the stiffness ratio.**

Keywords—**Compliant mechanism, Closed form Pressure balancing, Stiffness ratio, rotational hinge.**

I. INTRODUCTION

Conventional mechanical systems with assembled joints and rigid links usually possess undesirable properties such as backlash, friction and abrasion during motion [1]. Compared to conventional mechanisms, compliant mechanisms provide motion without friction, backlash, stick-slip, or wear [2]. Compliant mechanisms rely on elastic deformation and continuous displacement to transfer force or motion [3]. Their monolithic design ensures a compact structure and avoids system assembly errors. They are widely used in engineering applications where high positioning accuracy is required, such as scanning tunneling microscopes, precision positioning stages, X-ray lithography, and wafer alignment in microlithography [4], [5], [6]. Generally, compliant mechanisms are cheaper to fabricate than conventional high precision mechanisms which feature rigid joints [7].

Flexure hinges are typically constrained to a single-axis rotation and are widely utilized in precision positioning applications [8]. Conventional flexure hinges have a limited range of motion constrained to a few radians [9], [10]. Potentially, many more applications could benefit from similar mechanisms if they would posses a larger range of motion and higher load capacities. Currently, this search has resulted in more complex flexure designs (e.g. [11], [12]) or an increased number of joints in the mechanism (e.g. [13], [14]). To exceed the performance of the state of the art compliant hinges we want to enhance the range of operation for the compliant hinge. The range of operation is the difference between the normal- and rotation-stiffness. To increase the
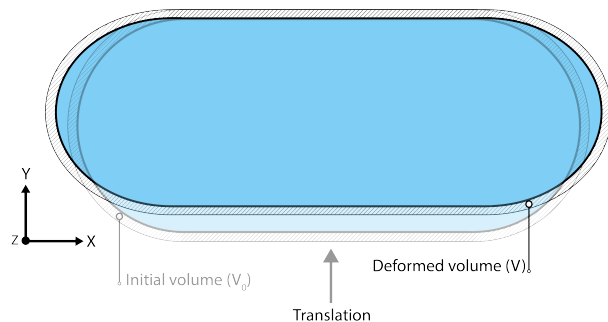
(a) Schematic overview of normal deformed shape to the initial shape of the hinge.
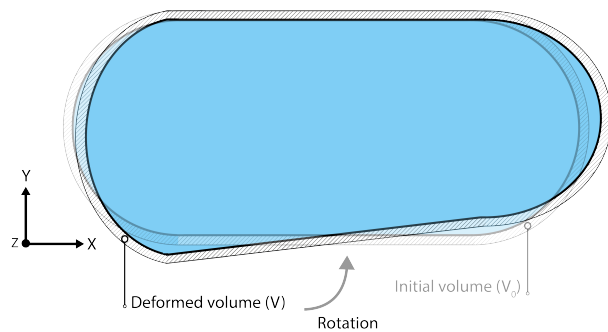
(b) Schematic overview of rotational deformed shape to the initial shape of the hinge.

Fig. 1: Schematic overview of 2D hinge design for the initial volume and deformed volume due to a prescribed normal displacement (a) prescribed angular displacement (b).

range of operation the rotation stiffness of the compliant hinge needs to be reduced while maintaining the normal- or support-stiffness. The majority of compliant hinges are designed using solely solid elements. However, mechanical machine components have also been investigated that make use of the properties of fluids to obtain desired properties for flexure hinges. Mechanisms consisting of fluid chambers have been used as dampers to relocate energy from a dynamic system [15], or as concept hydrostatic bearing design which uses the pressurized film to obtain a form of pressure balancing [16] or as fluid chambers in aerostatic dampers [17].

In general, fluids can be considered incompressible. Water for example only has a compressibility of $4.59 \cdot E^{-10} Pa^{-1}$ for a temperature of $20°C$ [18]. This could also be observed by the bulk modulus which is relatively high at $2.2E^9 Pa$,

while inherently the shear modulus equals $0Pa$. The bulk- and shear-modulus could obtain high support stiffness under compression while maintaining a low rotation stiffness. This idea, defined in literature as closed form pressure balancing, is the basis for a new type of compliant hinge presented in this work.

The basic embodiment of such closed form is shown in Figure 1 and consists of a fluid chamber enclosed by an elastic boundary material. The resulting hinge should desirably have a high normal-to-rotation stiffness ratio, in this work defined as performance. This dimensional ratio is defined in this work as,

$$\lambda_r[\theta/m^2] = \frac{K_n[N/m]}{K_r[N \cdot m/\theta]} \tag{1}$$

Where K_n represents the normal stiffness and K_r the rotation stiffness. In literature, an overview of the performance of existing compliant hinges has been presented using these two stiffness measurements [19], see figure 2.
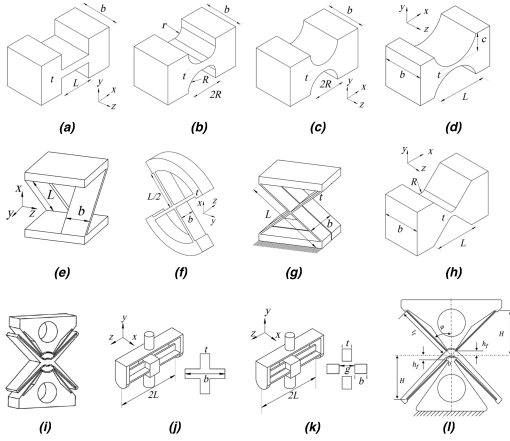

Fig. 2: Visualised overview of the conventional single-axis flexure hinges utilized in this work [19].

The performance of the selected conventional hinges in terms of stiffness is presented in Table I. The specific size of the hinges is based on a design space of an equally edged cube of $0.025m$.

What can be observed from Table I is that a trade-off is made between a high normal- or support-stiffness (K_n) or a high stiffness ratio (λ_r). And even then, the ratio is limited to a maximum in the order of $\lambda_r = 500$.

The objective of this paper is to introduce a new design of a compliant hinge, that improves on these stiffness characteristics. First the conceptual design of the closed form, geometric parameters, external boundary conditions and model stiffness are established in section II. A 2D finite element model (FEM) is used to determine the hinge characteristics. Using the 2D FEM model, a parameter sensitivity analysis is performed on parameters *l, h, t*. The global 2D parameter sweep, 3D FEM model and the measurement approach of the demonstrator are introduced in section III. Next, the results of the simulations

TABLE I: Overview of the stiffness ratio, normal- and rotation-stiffness of the conventional compliant hinges as presented in Figure 2.

Design	K_n [N/m]	K_r [$N \cdot m/\theta$]	λ_r [θ/m^2]
A	77.78	6.481	12.001
B	-	0.112	-
C	152.11	23.342	6.517
D	164.64	7.103	23.18
E	4.2	0.0079	531.65
F	16.8	0.0315	533.33
G	4.2	0.0078	538.46
H	94.99	34.142	2.782
I	2.1	0.021	100.0
J	10.76	0.0941	114.35
K	2.7	0.126	21.43
L	4.2	0.047	89.36

and subsequent measurements are shown in section IV. Finally, sections V & VI discuss and conclude the found developments and present the limitations of the model.

II. METHODS

To obtain insight in the behaviour of this new type of hinge, a 2D model is introduced. Figure 3 presents a schematic 2D overview of the basic embodiment, consisting of three geometric parameters,

- Length l is the distance between the left edge (dot) and right edge (dash) of the parallel walls.
- Height h is the distance between the upper (dash-dash-dot) and lower (line) edge of the parallel walls.
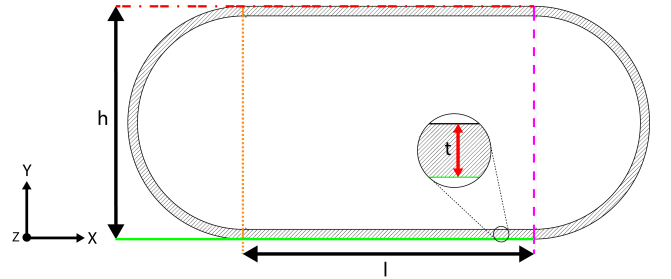- Thickness t is the dimension across the width of the wall.

Fig. 3: Schematic overview of 2D hinge design and the indicated geometric parameters. The various coloured lines indicate the dimensions of the geometric parameters as described above.

The outer surface of the curved sides is defined by a semicircle with radius $\frac{h}{2}$. The initial thickness t remains constant over the entire geometry. In this model, the used encapsulating body material is homogeneous isotropic linear elastic, following Hooke's law [20]. Since the fluid chamber within the compliant hinge is enclosed and the fluid is assumed incompressible, the inner volume remains constant throughout deformation. This is defined as follows,

$$(\frac{V}{V_0}) - 1 = 0 \tag{2}$$

Here V_0 is the initial volume. The deformed volume V should remain equal to V_0 for the assumption to hold, while the shape of the inner boundary changes. The change of the inner boundary is caused by the two actuation states resulting in the normal- and rotation-stiffness. A schematic overview of the boundary alterations, regarding a prescribed normal displacement and prescribed angular displacement are shown in Figure 1.

The deformed volume V is calculated using Gauss's theorem [21]. Gauss's theorem states that a closed surface is equal to the volume integral of the divergence over the region inside the surface,

$$\iiint\limits_V (\nabla \cdot \vec{F})dV = \oiint\limits_S (\vec{F} \cdot \vec{n})dS \tag{3}$$

Here $\vec{F}$ represents the 3D vector field of deformed surface and $\vec{n}$ states the normal vector on the inner surface. The schematic representation of the vectors is shown in Figure 4.
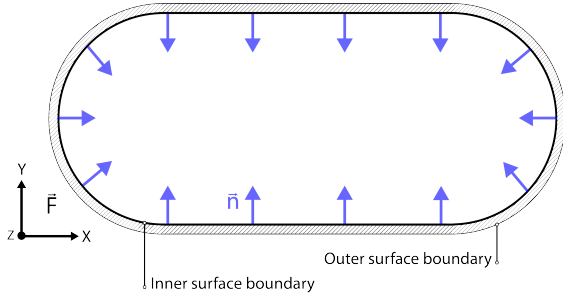

Fig. 4: Schematic overview of 2D hinge design for the static vector field $\vec{F}$ of the boundary material and the normal vectors $\vec{n}$ located at the inner boundary of the hinge.

Using Gauss's theorem we find the following equation regarding the deformed volume of the hinge,

$$V = -\int \frac{(n_x \cdot x + n_y \cdot y + n_z \cdot z)}{3} \tag{4}$$

In equation 4 the material vector field $\vec{F}$ is divided in components X, Y and Z. Each component represents a scalar part of the field vector $\vec{F}$ for the global coordinates system. Similar, normal vector $\vec{n}$ is divided in components n_x, n_y and n_z. Next, the initial pressure P inside the hinge is by definition not equal to the atmospheric pressure. The pressure inside the hinge is determined by the water inside the hinge as seen in Figure 5. After that, any variation to the initial shape of the hinge induces an internal pressure increase. The increase in pressure causes the boundary material to elongate whereas a specific stiffness is induced on normal- or rotation-deformation.

A. EXTERNAL BOUNDARY CONDITIONS

To design the hinge towards certain requirements, a set of boundary conditions is applied. The model is displacement controlled, meaning that a prescribed displacement is defined on the surface of the proposed hinge. The prescribed normal
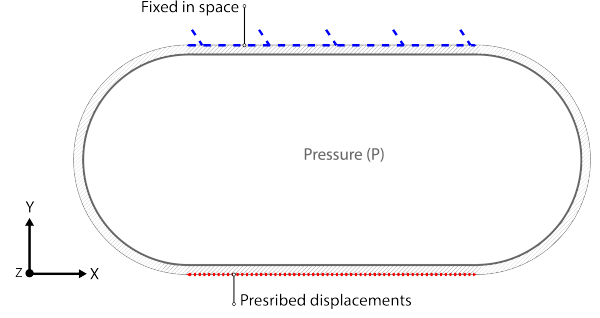

Fig. 5: Schematic overview of 2D hinge design and the internal pressure P, prescribed displacements and fixed boundary. The prescribed displacement is defined on the lower surface (dot). The upper surface of the top wall (dash) is fixed in space, opposing the actuated surface.

displacement (Figure 1a) is actuated in the direction of the positive Y-axis. The motion in both the $X-$ and Z-direction is constrained. In the same way the prescribed rotation (Figure 1b) is actuated around the positive Z-axis, inducing a counter-clockwise rotation. Translation in X, Y and Z-direction is constrained. For both displacements the actuated surface is selected rigid. The effect of the deforming material and enclosed fluid will constitute the total behaviour of the compliant hinge.

B. MODEL STIFFNESS

The stiffness model of the hinge constitutes the basis of modelling the performance. The stiffness is defined by three different deformations: Compression, rotation and lateral shear. The lateral deformation of the hinge is not considered in this study, since the stiffness is predominantly defined in the 3D hinge by shear stiffness of the front and back plane of the hinge, as a result, substantitily higher than the rotation stiffness, which is the results of the bending stiffness of the outer shell of the hinge. The normal- and rotation-stiffness are defined as follows,

$$K_t = \frac{F}{\delta} \tag{5}$$

$$K_r = \frac{\frac{l}{2} \cdot F}{\theta} \tag{6}$$

The force (F) is obtained by the surface integral of the traction (N/m^2) in the direction of the force [22]. The rotation stiffness is calculated using the integral of the traction multiplied by the arm $(M = F \cdot l)$. To obtain a high stiffness ratio, low bending stiffness and high hoop stiffness are required. Particularly the thickness parameter t greatly effects the general behaviour. The wall thickness t should not be large in comparison to the fluid volume. If it does, the physics of the hinge will tend more to behave like a pure elastic solid body. The magnitude of the fluid volume should not be much larger than the wall thickness t, where the hinge will tend to behave similar to the fluid properties, e.g. like a balloon.

Since the normal deformation δ is applied perpendicular to the rigid bottom surface of the hinge (positive Y-axis), the prescribed normal displacement is made relative to the height h of the hinge and is defined using equation 7,

$$\delta = \lambda_f h \tag{7}$$

The geometric height is indicated by parameter h. The prescribed displacement is denoted as a percentage of the height h and is described by λ_f. In order to compare the normal- and rotation-stiffness, both relative displacements should equal magnitudes. The angular displacement is defined by the arc length for the edge of the bottom surface, perpendicular to the rotational axis (Z-axis). The edge displacement is equal to,

$$\delta = \frac{l}{2}\theta \tag{8}$$

The prescribed rotation θ is applied at the centre line of the actuated surface and is defined as,

$$\theta = \frac{h \cdot 2\lambda_f}{l} \tag{9}$$

The prescribed rotation θ is dependent on the variation in height h and length l. Since the edge displacement of the bottom surface is dependent on a change in angle to induce a displacement relative to the height h.

C. 2D PARAMETER SENSITIVITY ANALYSIS

A 2D parameter sensitivity analysis is performed to observe the behaviour of the individual parameters. The range of variation was selected to cover two orders of magnitude for the selected ratios between the individual parameters. These ranges are based on various exploratory simulations regarding the convergence and stability of the solutions,

- $1 \leq \frac{l}{h} \leq 100$
- $1 \leq \frac{h}{t} \leq 100$

We found that multiple configurations within the boundary range induce non-feasible deformations, due to small stiffness magnitudes or internal collision of the elastic boundary to the structure of the hinge. Therefore, an adaptive range was set up,

- $2.5 \leq \frac{l}{h} \leq 4$
- $4 \leq \frac{h}{t} \leq 10$

These ranges provide insight on the general behaviour of the compliant hinge besides a stable working range for the numerical model. Prior to the parameter sensitivity analysis, an initial geometry was chosen, based on an exploratory parameter search, to set the other variables during identification of a single parameter. The chosen range is limited by the boundary range of the conventional compliant hinges, as we set the range of the length l to, $10mm - 25mm$. Consecutively the ranges of the height h, $6.25mm - 10mm$ and the thickness t, $1mm - 2.5mm$ are determined by the selected parameter ratios, based on the upper limit of each parameter variation. The initial geometry was selected in the middle of these selected ranges. As mentioned before, these values are set up by means of physical requirements and are solely used to center the parameter sensitivity analysis.

The finite element simulation is based on a linear elastic material model, making only the ratio between the geometric parameters relevant. The profile of the individual parameter variation does not depend on the material properties (E, ν, ρ), thus the magnitude of these properties is irrelevant. Consequently, the Y-axis is scaled to indicate the stiffness on the initial design of the compliant hinge. The course of the stiffness profiles are of interest to design the compliant hinge. The 2D parameter sensitivity analysis determines the effect of variation for each geometric parameter.

First the variation over the length l is presented in Figure 6a, showing a change in normalized stiffness magnitude. The normal stiffness increases linear for an increase in length l, while the rotation stiffness increases non-linear for an increase in length l. We would expect that both stiffness profiles are different, as the discrepancy between the normal- and rotation-stiffness is largely dependent on the length l of the hinge.

(a) Variation of length l for stationary geometric parameters h and t.

(b) Variation of height h for stationary geometric parameters l and t.

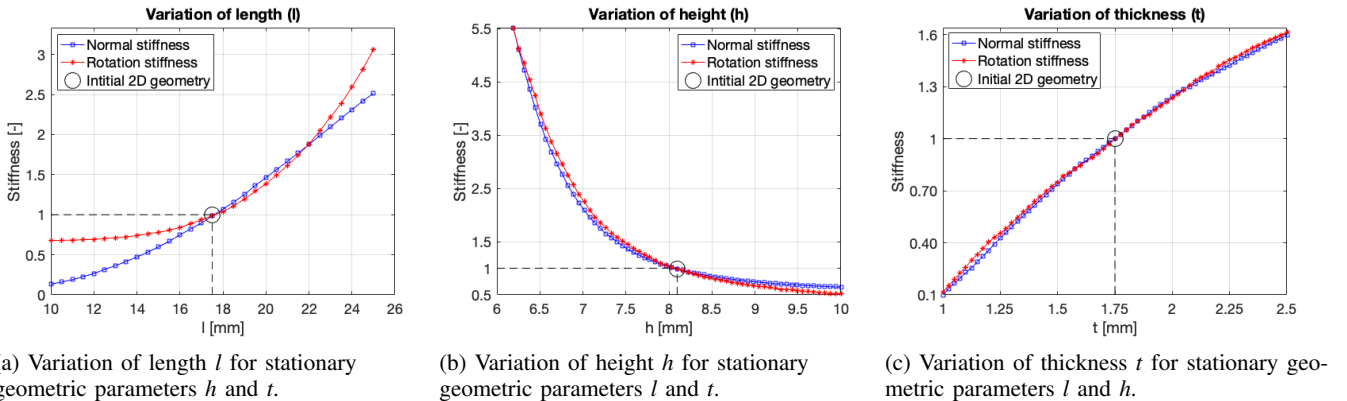(c) Variation of thickness t for stationary geometric parameters l and h.

Fig. 6: Overview of individual 2D parameter sensitivity analysis of the three geometric parameters l (a), h (b), t (c), displayed on the X-axis. The Y-axis indicates a dimensionless stiffness as both the normal- and rotation-stiffness. The stiffness on the initial 2D hinge geometry is shown as a benchmark.

4

Secondly, the variation over the height h is presented in Figure 6b. The shape of both stiffness profiles is approximately similar. Nevertheless, the plot shows a discrepancy between both stiffness profiles. We would expect that both stiffness profiles are similar.

Finally, the thickness t is varied in Figure 6c. The plot shows a small difference between the normal- and rotation-stiffness. We would expect that both stiffness profiles are similar.

III. CASE STUDY

A case study is performed to analyse the performance of the pressure balanced hinge. First a 2D parameter sweep has been performed to the geometric parameter values of the given 2D boundary design. The normal- and rotation-stiffness should be related to the conventional stiffness magnitudes based on the following statements,

- 100 N/m $< K_n$ of the proposed hinge

- 10 N·m/$\theta > K_r$ of the proposed hinge

Where the required stiffness values are based on the rounded average stiffness magnitudes of the conventional compliant hinges (Table I). The statements prevent the hinge from a high rotation stiffness, as a high performance could be obtained for high rotation stiffness and even higher normal stiffness.

Furthermore, the FEM model makes use of a non-linear solver and geometric non-linearity. The relative tolerance used in FEM solver is $1E^{-3}$. The parameter space defined by the triplet X, Y, Z is uniformly discretized in a 19 x 19 x 19 space. For the parameter sweep we make use of the same geometric ranges as for the parameters sensitivity analysis.
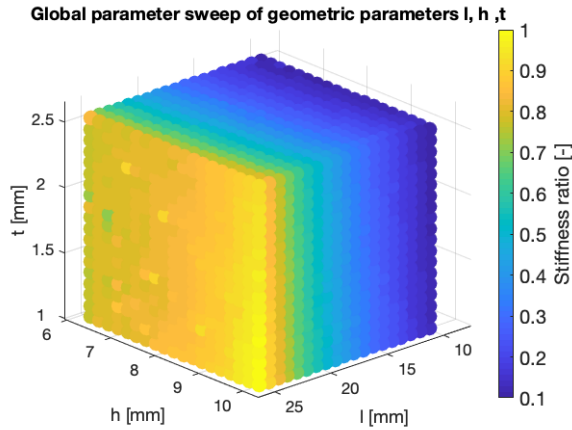

Fig. 7: Overview of the global parameter sweep of the three geometric parameters l, h, t. The high performances are located at the plane $l = 25mm$. The stiffness ratio is scaled to the interval [0.1,1].

From the results, the highest performances within the boundary range are located at the boundaries of the parameter sweep. This is clarified in Figure 8, were three intersected views of the global parameter sweep are shown. For the total variation over the thickness t, the results are in close correspondence. The first thing that clearly stands out in Figure 7 is

the pattern on the left side for variation in height h, thickness t and length $l = 25mm$. Some calculation points show diverging colours to the descending colour panel. The divergence is the result of the transition between the edge of the actuated surface and the side of the hinge during deformation. Elements is this region are deforming significantly, causing numerical errors and a limited range of deformation for the performed parameter sweep in FEM.
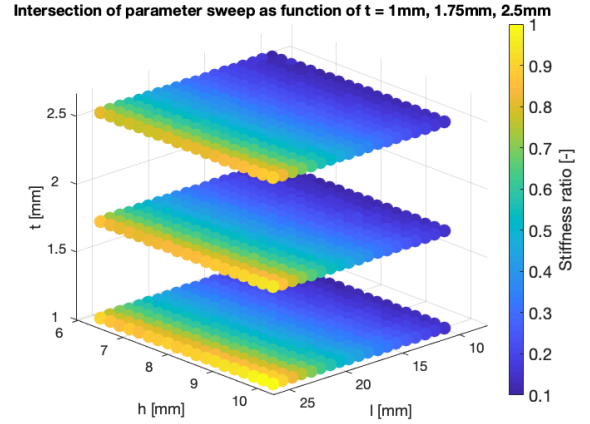

Fig. 8: Intersected view of the global parameter sweep. The high performances are located at the boundary of the parameter sweep. The stiffness ratio is scaled to the interval [0.1,1].

The highest performances in the selected boundary range are found for large length l, height h and a small thickness t. To partially validate the design of the hinge two configurations of the 2D model are selected within the feasible boundary range. The selected designs are chosen based on the highest performances within the parameter sweep. The configurations are located at the upper- and bottom-limit of the variation over the thickness t in the global parameter range. The chosen configurations are defined as follow: $\frac{l}{h} = 2.5, \frac{h}{t} = 4$ and $\frac{l}{h} = 2.5, \frac{h}{t} = 10$, respectively.

The calculations in the design space were performed within the design space of 25 x 25 x 25mm, similar to the design space of the conventional compliant hinges shown in figure 2. The dimensions for the experimental demonstrator were subsequently enlarged by factor 2 to ensure the feasibility of the demonstrator. Therefore, the selected feasible boundary range of the demonstrator comprises a cube with equal edges of $0.05m$. The dimensions of both configurations are show in Table II,

TABLE II: Geometric parameters of the 2D hinge design for the two most promising configurations of the demonstrator.

Parameter	Configuration 1	Configuration 2
l	0.05 m	0.05 m
h	0.02 m	0.02 m
t	0.005 m	0.002 m

The magnitudes of the height h and thickness t are based on the previous selected mutual ratio between the geometric

parameters and are limited by the constrained magnitude of the length $l = 0.05m$.

A. DEMONSTRATOR

A detailed 3D analysis of the hinge is obtained to determine a more accurate performance. Figure 9 shows a partly intersected view of the 3D hinge, introducing a depth dimensions d. For the transition of 2D to 3D, the newly added curves front and back of the hinge are similar to the curves at the side. The newly added corners are designed as a quarter sphere. The introduction of the additional parameter d influences the normal- and rotation-stiffness of the hinge as can be seen in Figure 10.
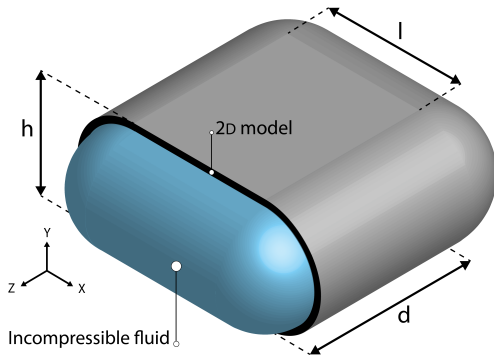

Fig. 9: Intersected 3D view of the compliant hinge for an additional parameter: depth d. The black outline indicates the 2D hinge design shown in Figure 1.
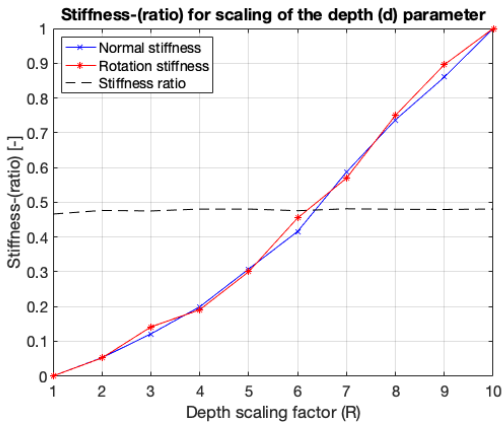

Fig. 10: Plot of depth scaling factor R for the stiffness ratio, normal- and rotation stiffness of the 3D FEM model. The 2D geometric parameters (l, h, t) are kept constant during deformation.

For this selected range of different depth values, the stiffness ratio remains approximately constant. Subsequently, the performance of the detailed 3D model is defined. The hinge allows for large (non-linear) deformations, but in the model we have limited the deformations to be small, linear. In order to ensure numerically stable calculations, the relative

displacement is limited to less than 6.25% of the height h. We assume that the depth d is equal to length l of the hinge to fulfil the feasible design space. Since the stiffness profiles are approximately constant, the slope of the traction forces provide a more sufficient benchmark. The traction forces corresponding to the normal- and rotation-displacement on both configurations are presented in Figures 11 & 12. The traction force on the 2D FEM model is used for an assumed depth of the hinge of $50mm$, similar to the 3D FEM model.

Fig. 11: Plot of the traction forces for the normal displacement of the 2D- & 3D-FEM model comprising the first- and second-configuration. The traction forces on the 2D- and 3D-FEM models are calculated for a depth of $0.05m$.

The normal forces of both configurations decrease with the transition from 2D to 3D. The normal force of the 3D FEM model is approximately 40% lower compared to the normal force of the 2D FEM model.
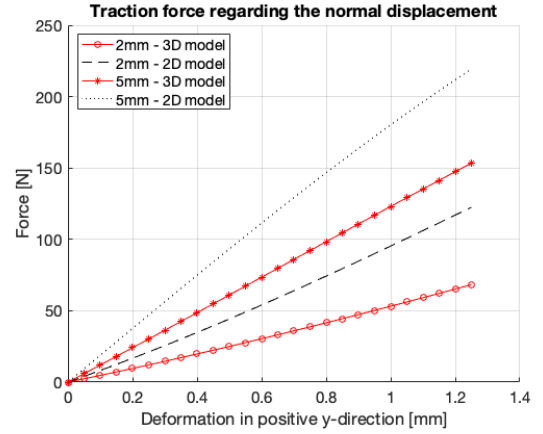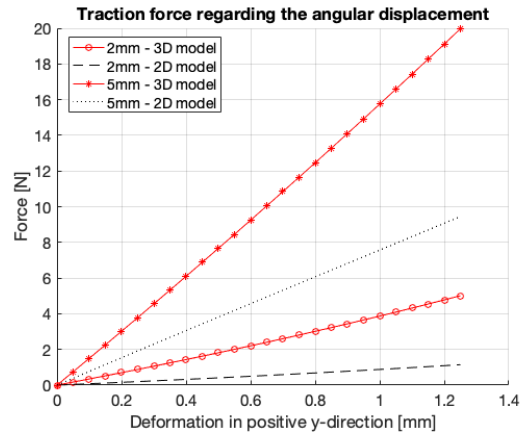

Fig. 12: Plot of the traction force for the angular displacement of the 2D- & 3D-FEM model comprising the first- and second-configuration. The traction forces on the 2D- and 3D-FEM models are calculated for a depth of $0.05m$.

In Figure 12 the rotation forces of both configurations are shown. The rotation force of the 3D FEM model is significant

higher compared to the rotation force of the 2D FEM model. Overall, the stiffness ratio of the 3D FEM model is lower compared to the stiffness ratio of the 2D FEM model, for both configurations. Now the effect of the depth R is known, the geometric scaling S needs to be examined.

B. GEOMETRIC SCALING

The effect of geometric scaling is of interest to fit the conventional applications. Scaling the geometric parameters (l, h, t) scales the performance of the hinge. During scaling the various ratios between the geometric parameters are kept constant, the shape of the hinge remains similar. The effects of scaling are shown in Figure 13.
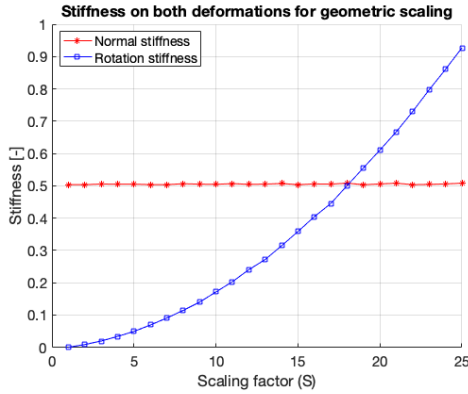
(a) Plot of normal- and rotation-stiffness for an increasing geometric scale S. During the measurement the depth d is kept constant.
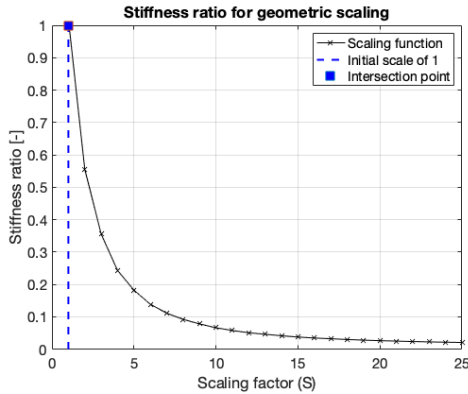
(b) Scaling function for an increasing geometric scale (S). During the measurement the depth d is kept constant.

Fig. 13: Overview of the stiffness profiles for an increasing geometric scale. (a) The course of the normal- and rotation-stiffness for an increase in geometric scale. (b) The scaling function is applied to the initial 3D hinge design.

In Figure 13a the development of the normal- and rotation-stiffness are shown for scaling of the geometric parameters (l, h, t). The scale factor S is obtained by dividing the calculated normal- to the rotation-stiffness, respectively. Figure 13b provides the scale factor S as a function of the performance, having an magnitude of approximately $\frac{1}{S}$.

C. MEASUREMENT MODEL

The experimental study is divided into two steps: fabrication of the hinge and experimental test setup.

FABRICATION

To partially validate the concept, a demonstrator is produced. In order to manufacture the encapsulating body, a castable silicone material is selected [23]. We assume that the bonding region of silicone to silicone possesses similar material properties as the silicone material [24]. The used silicone has a shore hardness of A40. To determine the material properties, as used in the FEM model, an *ISO:37* tensile strength test is performed [25].
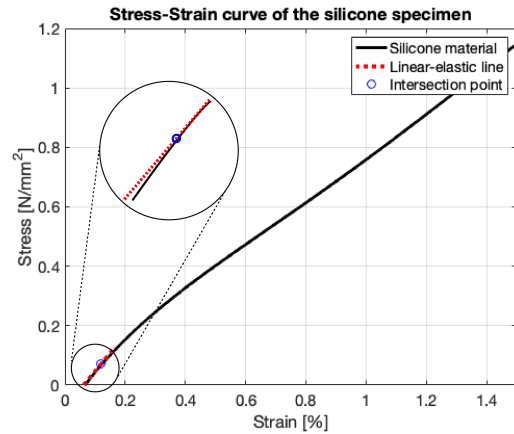
Fig. 14: Stress-strain curve of the silicone material. The region of interest is the slope for small deformations (1% Strain). The window shows an enlargement of the tangent linear-elastic line.

Figure 14 shows the stress-strain curve of the silicone material. To simplify the calculations, the Young's modulus E is defined from a tangent linear elastic material model at 1% of the strain. The specimen of the tensile test and the hinge are produced in different runs, the material properties may vary. Therefore a range of 15% [26] for the Young's modulus is used: $1.2 \pm 0.18 MPa$. The selected Young's modulus for the detailed 3D FEM model is $1.061 MPa$, while we assume a Poisson ratio of 0.49 for the hyperelastic silicone [27], [28].

The mold is designed for a castable material and fabricates half the closed form, shown in Figure 15.

Figure 15 shows on the left the total mold assembly consisting of three parts: The top, the middle and the bottom. The top and bottom part together form half the compliant hinge. The middle part creates pocket in one half of the hinge. The other half is produced without pocket to create a large opposing surface. The hinge is filled with room temperature tap water ($\sim 20^\circ C$), by an injection needle. Alternately, another needle is used to extract the air inside the hinge, using the same injection spot on the surface of the hinge. Both needles are similar and have a diameter of $0.6mm$, causing the material layer to remain impermeable after retraining.

Fig. 15: An overview and section view of the mold assembly. On the left the three different mold components and the total assembly. On the right three cross section views of the side-, top- and intersected-view, respectively.
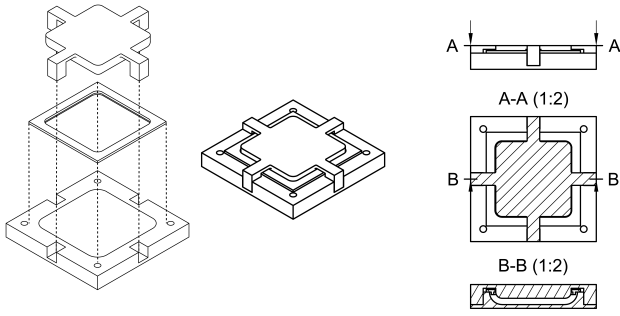
D. JOINT CONNECTOR

To measure the traction forces on the demonstrator, a connector is required between the hinge and the testing machine. The connector should provide the surface rigidness simulated in FEM. Since we want to avoid bonding to the silicone, to prevent bonding effects in the measurement results, a specific joint connector is designed. To clarify the working principle, Figure 16 shows a cross section of the joint connector.
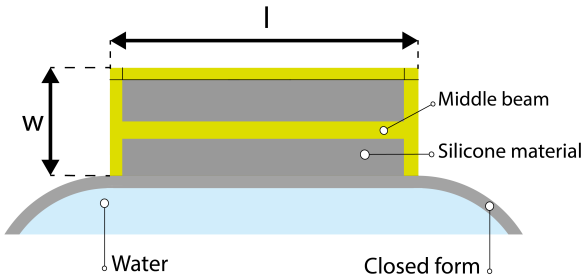

Fig. 16: Schematic cross section view of the joint connector attached to the compliant hinge, indicating the used dimensions. The intersection is located along the middle of the depth d.

Here, the magnitudes of parameter l and the depth d are equal to the parameters used in Figure 9. The height of the connector is denoted by parameter w, which is equal to $0.02m$. The connector is 3D printed by PLA material. The bottom holds an open surface enclosed by the boundary material of the connector.

To attach the joint connector to the hinge, the silicone is casted in the extruded part on top. Inside the extruded part, a middle beam is connected to the joint connector, covering approximately $\frac{1}{3}$ of the surface area. The silicone enclosed middle beam prevents the joint connector from separating to the hinge in the X, Y and Z-direction. The square shape of the connector prevents rotation around the X, Y and Z-axis, constraining the joint connector for undesirable displacements.

A Zwick-Roell Z005 tensile test bench is used to perform the measurement on the normal- and rotation-displacement. The experimental setup of the machine for the normal displacement is shown in Figure 17.
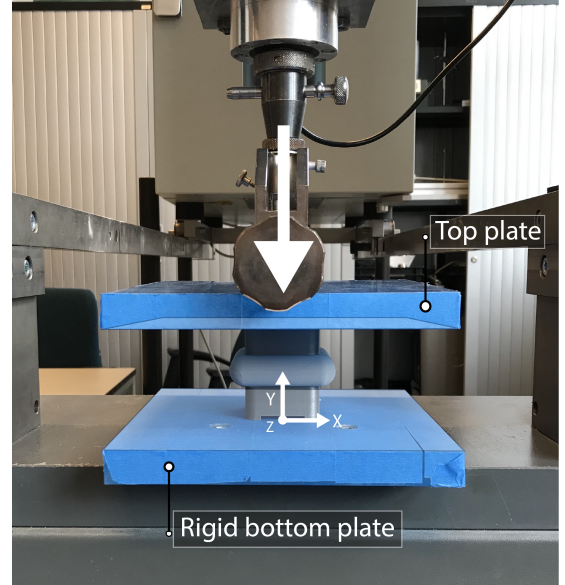
Fig. 17: An overview of the experimental test setup for a normal deformation which is applied by two horizontal plates. The Figure also shows the testing machine.

The hinge is enclosed between two horizontal plates. The top plate is connected to the testing machine, while the bottom plate is rigidly fixed to the world. Actuating the top plate in the negative Y-direction provides the normal deformation of the hinge. The experimental test setup for the rotation is shown in Figure 18.

The rotational measurement results are obtained by two plates, a horizontal bottom plate and a vertical top plate. To induce a moment on the compliant hinge, the vertical top plate applies a force perpendicular to the joint connector of the compliant hinge. The distance from the point of force application to the geometric center of the hinge introduces the mechanical moment on the hinge.

IV. RESULTS

To validate the proof of concept all examined models are compared. This is done by means of the stiffness ratio, normal- and rotation-force. For both configurations, shown in Table II, the measurement on the demonstrator is repeated 3 times. The repeated measurement results for the normal force exhibit a maximum difference of approximately 1%. For the measurements on the rotation force the tip of the top plate glides along the rough surface of the joint connector, causing irregularities in the measured data. Therefore, the three measurements of both prescribed displacements are curve fitted to the measured traction forces, showing a maximum difference
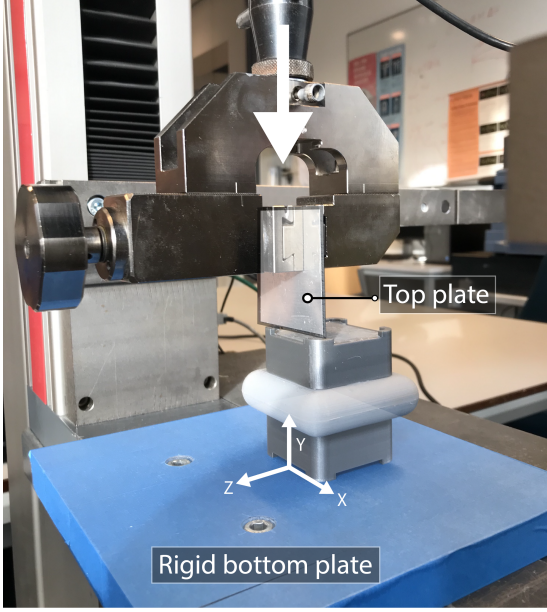
Fig. 18: A side overview of the experimental test setup for rotational deformation which is applied by a horizontal bottom plate and a vertical top plate. The Figure also shows the testing machine.

of approximately 1% at maximal displacement. The curve fitted traction forces as measured in the first configuration ($t = 5mm$) are shown in Figure 20.

The curve fitted traction forces of the 3D FEM model and the demonstrator are in close correspondence for both deformations ($\pm 10\%$). In Figure 21 the curve fitted traction forces of the second configuration are shown.

Again, the results of the 3D FEM are in close correspondence to the measurement results on the demonstrator ($\pm 10\%$). To determine the performance of the proposed hinge, the overall stiffness ratio of the demonstrator is compared to the stiffness ratio of the the conventional compliant hinges (Table I). The overall performance of the three examined models are shown for both examined configuration in Figure 19. The Figure on the left shows the performances of the first configuration. As shown, the performance of the 3D FEM model and the demonstrator are in close correspondence. The Figure on the right shows the performances of the second configuration. Again, the performance of the 3D FEM model and the demonstrator are in close correspondence. Therefore, it is said that, all the measurement results on the demonstrator are in close correspondence to the measurement results of the 3D FEM model. The magnitudes of the performances are summerized in Table III,

To finally compare the performance of the conventional compliant hinges, to the performance of the proposed hinge, the design space of the conventional compliant hinges should be adhered to. Since the 3D-FEM model is validated, the model can be used to calculate the traction forces on every sized model. Therefore, the stiffness magnitudes of the 3D

TABLE III: Measurement results of the two promising design configurations for 2D- & 3D-FEM models within the feasible boundary range of the demonstrator. The performances of the 2D- & 3D-FEM models are shown for unit [rad/m^2].

	Configuration 1	Configuration 2
2D - Stiffness ratio	3.71+04 rad/m^2	1.71e+05 rad/m^2
3D - Stiffness ratio	1.23e+04 rad/m^2	2.13e+04 rad/m^2

FEM model are used to obtain the stiffness ratio for the proposed hinge regarding the design space of the conventional compliant hinges, shown in Table IV,

TABLE IV: Measurement results of the two promising design configurations for 2D-, 3D-FEM models within the design range of the conventional compliant hinges. The performances of the 2D- & 3D-FEM models are shown for unit [rad/m^2].

	Configuration 1	Configuration 2
2D - stiffness ratio	7.89e+04 rad/m^2	3.42e+05 rad/m^2
3D - stiffness ratio	1.69e+04 rad/m^2	2.18e+04 rad/m^2

The performance of the conventional compliant hinges (Table I) is compared to the performance of the proposed hinge (Table IV). If we analyse the magnitude of the stiffness ratio for the conventional compliant hinges and the 3D FEM model of the proposed hinge, we find that the largest state of the art stiffness ratio is increased by a factor of 30 and 40 for configuration 1 and 2, respectively. These factors are based on the best performing conventional hinge G, visualized in Figure 2. The performance of this conventional compliant hinge is $538.46\theta/m^2$.

V. DISCUSSION

Following the structure of the detailed design, the results and analysis of the measurements on the demonstrator are discussed. Each section will be discussed in terms of found result, assumptions and simplifications.

A. HINGE DESIGN

In the transition from the 2D- to the 3D-model we have observed that the additional side curves and the corners of the 3D model have an attenuating effect on the normal force of the hinge and an enhancing effect on the rotation force. The total inner surface of the side curves around the 3D model of the hinge is significant larger compared to the inner surface of the side curves of 2D FEM model. As the actuated force on the hinge is divided over the inner surface, the boundary material of the hinge elongates. For the 2D model the water diffuses over a smaller surface for which the boundary material extends even more, having a larger stiffness for the same actuated force. Furthermore, the bending stiffness of the additional curves and corners enhances the rotation stiffness of the 3D model over the 2D model.

The aim of the design is focused towards a large range of operation, thereby the goal to increase the range of motion of this hinge has not been considered in this research. In practice the geometric size of the hinge determines the potential angle
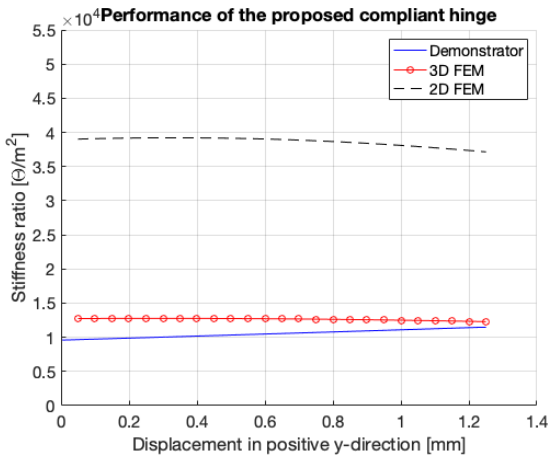
(a) Plot of stiffness ratio for the 2D- & 3D-FEM models and demonstrator for configuration 1.
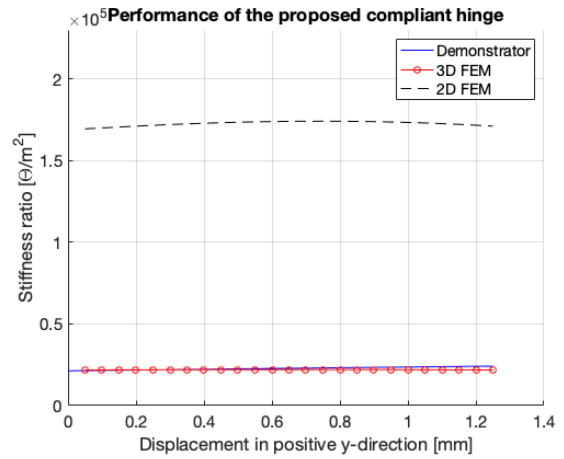
(b) Plot of stiffness ratio for the 2D- & 3D-FEM models and demonstrator for configuration 2.

Fig. 19: Overview of the performance of the 2D- & 3D-FEM models and the demonstrator. (a) The performances of the first configuration ($t = 5mm$). (b) The performances of the second configuration ($t = 2mm$). All performances are obtained for a displacement of 6.25% of the height h of the demonstrator.
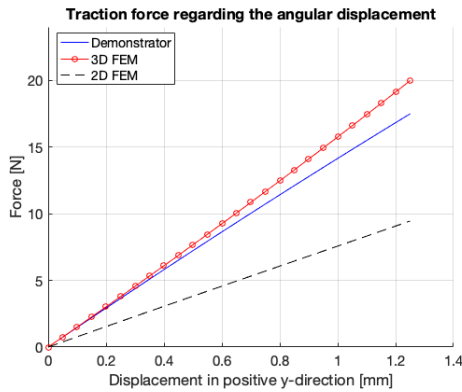
(a) Normal forces of configuration 1.

(a) Normal forces of configuration 2.

(b) Rotation forces of configuration 1.
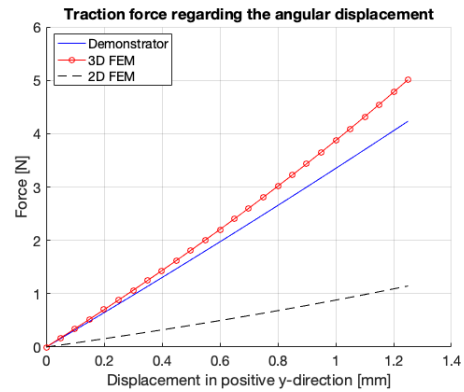
(b) Rotation forces of configuration 2.

Fig. 20: Plots of the normal- and rotation-forces for the 2D- & 3D-FEM models and the demonstrator, which has a wall thickness of $t = 5mm$ (Configuration 1). The traction forces are obtained for a displacement of 6.25% of the height h of the demonstrator.

Fig. 21: Plot of the normal- and rotation-forces for the 2D- & 3D-FEM models and demonstrator, which has a wall thickness of $t = 2mm$ (Configuration 2). The traction forces are obtained for a displacement of 6.25% of the height h of the demonstrator.

10

of rotation, as the rotation is limited by the internal collision of the body. The proposed hinge design is not able to provide a larger angle of rotation for the same input force as conventional compliant hinges. However, the operational range of the proposed hinge is at least a factor 30 larger than the operational range of the best performing conventional compliant hinge, providing many potential applications for the proposed hinge, including: Hydrostatic bearings, force distribution system and moving architecture, including stadium doors [29], [30], [31].

B. MEASUREMENT

The measurements show that the traction forces on the demonstrator are in close correspondence with the traction forces of the 3D FEM model. The traction forces on the demonstrator deviates a maximum of 10% to the traction forces on the 3D FEM model. The close corresponding traction forces could confirm that the 3D FEM model is similar to the realized demonstrator. Confirming that the joint connector induces a rigid connection between the experimental test setup and the proposed hinge.

For the actuation on the demonstrator we observed a line symmetry through the center of the hinge. The symmetry causes the top plate of the testing machine to move the prescribed distance whereas the surface on top and bottom of the hinge are displaced half the distance of the prescribed displacement. The study showed that, due to the symmetry, the hinge holds the same physics on deformation.

The pressure of the enclosed water was not observed to decrease during the experiments, as the measurement results were nearly similar, which suggest that there is little to no leakage of water during deformation of the hinge.

We only looked at small deformations because of the limitations in the FEM model. For the maximal displacement of 6.25% of the height h, the hinge does not fail, which confirms the assumption that the bonding of the silicone to silicone for small deformations remains intact. Large deformations become relevant when the geometric size of proposed hinge is enlarged. However, further research towards the maximum angle of rotation, load capacity and the geometric design of the hinge are recommended.

C. PERFORMANCE

The performance of both demonstrators are in close correspondence with the performance of the 3D FEM model. The stiffness ratio on the demonstrator deviates maximal 5% to the stiffness ratio on the 3D FEM model. This variation in performance could originate from the material properties of the silicone, which can variate due to the composite of the mixture with the hardener. Also the applied rotation on the demonstrator is dependent for the performance, as the rotation should be aligned along the shortest distance across the surface of the hinge. Otherwise the rotation stiffness will increase and the performance of the proposed hinge decreases.

The rotation stiffness of the realized demonstrators of the new hinge is not lower than the lowest rotation stiffness of the conventional compliant hinges, as conventional hinge G

provides the lowest conventional rotation stiffness of $7.8E^{-2}$ $N \cdot m/\theta$. The rotation stiffness for the second configuration of the proposed hinge is $1.5 N \cdot m/\theta$, which is a factor 192 higher than conventional hinge G. On the other hand, the second configuration of the proposed hinge provides a large normal stiffness of $4.3E^4$ N/m, were conventional hinge D provides the highest conventional normal stiffness of $164.64 N/m$. The normal stiffness of the proposed hinge is a factor 261 higher than the largest normal stiffness of conventional hinge D. Comparing the factors of both stiffness results in the high performance of the hinge. For the first configuration the normal- and rotation-stiffness are even higher.

Although the measurement results and calculated FEM results are already in close correspondence, for the applied normal compression and the applied rotation, there is room for improvement in the applied rotation. In the current setup the force application point slides over the top plane of the hinge, causing some inaccuracies.

VI. CONCLUSIONS

The new design of the proposed hinge for a large operation range results into a hinge with relative large normal stiffness and relative low rotation stiffness compared to the average stiffness of the conventional compliant hinges. In this research the main objective was to enhance the performance of the conventional compliant hinges by introducing a new hinge design which utilizes incompressible fluid inside an elastic closed body to obtain the desired stiffness profile.

It has been demonstrated that the performance of the proposed hinge exceeds the performance of the state of the art. Here, the highest performance of conventional compliant hinges is compared to the performance of both demonstrator hinge configurations. The performance of the best conventional hinge G is exceeded by the first configuration for a factor 30 and by the second configuration for a factor 40. The increase in performance includes a larger range of operation. Due to limitations in FEM and the current design of the hinge only small displacements have been studied. Therefore, further research towards the increase in angle of rotation and the load capacity of the hinge are recommended. Overall, it is believed that the implementation of the proposed compliant hinge in current applications, in which a stiff compression and compliant rotation are required, will pave the way for the development of new compliant hinges based on closed form pressure balancing.

REFERENCES

[1] Lateş, D., Căşvean, M., Moica, S. (2017). "Fabrication Methods of Compliant Mechanisms," *Procedia Engineering*, 181, (1), pp. 221-225.
[2] Tian, Y., Shirinzadeh, B., Zhan, D., et al. (2010). "Three flexure hinges for compliant mechanism designs based on dimensionless graph analysis," *Precision Engineering*, 34, (1), pp. 92–100.
[3] Rowe, W.B. (2012). *Hydrostatic, Aerostatic and Hybrid Bearing Design*. Butterworth-Heinemann.
[4] Schitter, G., Thurner, P.J., Hansma, P.K. (2006). "Design and input-shaping control of a novel scanner for high-speed atomic force microscopy". *Mechatronics*, 18, (5–6), pp. 282–288.

[5] Miller, J.A., Hocken, R., Simith, S.T., et al. (1996). "X-ray calibrated tunneling system utilizing a dimensionally scale nanometer positioner". *Precision Engineering*, 18, (2–3), pp. 95–102.

[6] Choi, K.B., Lee, J.J. (2005). "Passive compliant wafer stage for single-step nano-imprint lithography". *Review of Scientific Instruments*, 76, (7). pp. 75–106.

[7] Howell, L.L. (2001). *Compliant Mechanisms*. New York, New York: Wiley.

[8] Callegari, M., Cammarata, A., Gabrielli, A, et al. (2009). "Analysis and design of a spherical micromechanism with flexure hinges". *Journal of Mechanical Design*, 131, (5).

[9] Lobontiu, N. (2002). *Compliant Mechanisms: Design of Flexure Hinges*. Boca Raton: CRC Press.

[10] Christen, G., Pfefferkorn, H. (1998). "Nachgiebige Mechanismen: Aufbau, Gestaltung, Dimensionierung und experimentelle Untersuchung". *VDI-Berichte*, 1423, pp. 309–329.

[11] Henein, S., Spanoudakis, P., Droz, S., Myklebust, L.I., Onillon, E. (2003). "Flexure Pivot for Aerospace Mechanisms". *European Space Agency*, (Special Publication) ESA SP-524.

[12] Fowler, R.M., Magleby, S.P., Howell, L.L. (2014). "Flex-16: A Monolithic Large-Displacement Compliant Rotational Hinge". *Mechanism and Machine Theory*, 82, pp. 203-217.

[13] Beroz, J., Awtar, S., Bedewy, M., Tawfick S., Hart A. J. (2011). "Compliant microgripper with parallel straight-line jaw trajectory for nanostructure manipulation". *Proceedings - ASPE 2011 Annual Meeting*, 52. pp. 90-93.

[14] Cosandier, F., Chatagny, V., Clavel, R. "Optimizing the Design of the 13-Hinge Rectilinear Stage for High Straightness Translation".

[15] Cohen T., Kurzeja P., Bertoldi K. "Architected squirt-flow materials for energy dissipation". (2017). *Journal of the Mechanics and Physics of Solids*, 109, pp. 22-33.

[16] Nijssen, J.P.A., van Ostayen, R.A.J. (2019). "Open Form Pressure Balancing for Compliant Hydrostatic Thrust Bearings". *Advances in Mechanism and Machine Science*, pp. 3965-3974.

[17] Nijssen, J., Diepeveen, N., Kempenaar, A. (2018). "Development of an interface between a plunger and an eccentric running track for a low-speed seawater pump".

[18] Fine, R.A., Millero, F.J. (1973). "Compressibility of water as a function of temperature and pressure". *The Journal of Chemical Physics*, 59, (10), pp. 5529-5536.

[19] Farhadi Machekposhti, D., Tolou, N., Herder, J. L. (2015). "A Review on Compliant Joints and Rigid-Body Constant Velocity Universal Joints Toward the Design of Compliant Homokinetic Couplings". *Journal of Mechanical Design*, 137, (3), pp. 032301.

[20] Hooke's law. Oxford Reference. Retrieved 14 Jan. 2020, from https://www.oxfordreference.com/view/10.1093/

[21] Katz, V.J. (1979). "The history of Stokes's theorem". *Mathematics Magazine*, 52, (3), pp. 146–156.

[22] Liu, I.S. (2002). *Continuum Mechanics*. Berlin, Heidelberg: Springer.

[23] Siliconenrubber-PS8540. Available [online]: https://www.polyservice.nl.

[24] de Buyl, F. (2001). "Silicone sealants and structural adhesives". *International Journal of Adhesion and Adhesives*, 21, (5), pp. 411–422.

[25] "ISO 37:2017 Rubber, vulcanized or thermoplastic — Determination of tensile stress-strain properties". Available [online]: https://www.iso.org/standard/53023.html.

[26] Van Lancker, B., Corte, W., Belis, J. (2016). *Material properties of a structural silicone for linear adhesive glass-metal connections*.

[27] Jung, J., Hwang, I., Lee, D. (2017). "Contact Pressure and Strain Energy Density of Hyperelastic U-shaped Monolithic Seals under Axial and Radial Compressions in an Insulating Joint: A Numerical Study". *Applied Sciences*, 2017, 7, (8), pp. 792.

[28] Pritchard, R.H., Lava, P., Debruyne, D., Terentjev, E.M. (2013). "Precise determination of the Poisson ratio in soft materials with 2D digital image correlation". *Soft Matter*, 9, (26), pp. 6037-6045.

[29] van Ostayen, R.A.J., van Beek, Anton., Ros, Mink. (2004). "The Hydro–Support: An Elasto–Hydrostatic Thrust Bearing with Mixed Lubrication". Tribology International, 37, pp. 607-616.

[30] van Willigen, N.J., Nijssen, J.P.A., van Ostayen, R.A.J. (2019). "Whiffletree-based deforming hydrostatic bearing".

[31] Mahovič, A. (2015). "Typology of retractable roof structures in stadiums and sports halls". *Scientific journal*, 3, pp. 90-99.

Discussion

The main objective of this thesis is to design a compliant hinge, based on closed form pressure balancing, having a larger performance than the selected conventional compliant hinges. In this Chapter the results of this research are discussed in a broad sense. First, the results of the paper and the main objective of this thesis are discussed. Subsequently, the appendices supporting the paper will be discussed.

5.1. Paper

This thesis has provided the required knowledge for the development of a new compliant hinge design, based on an enclosed fluid principle. The paper (Chapter 4) presents the design of a new type compliant hinge which utilizes water inside an closed silicone body to obtain a desired performance. The performance of the compliant hinge is defined by the normal-to-rotation stiffness ratio. Fundamental knowledge and FEM analysis have been used to measure this performance. The results of the FEM analysis showed a high performance over the range of geometric parameter *t* within the selected boundary range. Two configurations were chosen to be realized. These configurations are located at both ends of the boundary range, both having a high performance. Conventional hinge G provides the lowest conventional rotation stiffness of $7.8E^{-2}N \cdot m/\theta$, and a normal stiffness of $4.2N/m$, see Appendix C.2. The performance of this conventional hinge is $538.46\theta/m^2$. The performance of the proposed hinge exceeds the performance of the best conventional hinge by a factor 30 for the first configuration and by a factor 40 for the second configuration.

The literature provides a review about the analytical behaviour of the conventional compliant hinges. The hinge properties are analytically determined by various papers, including the range of motion, the normal- and rotation-stiffness. We assume that these analytical results are comparable to the measurement results on the proposed hinge, as the motions for compression and rotation are equal to the motion of the conventional compliant hinge. A point of interest is the range of motion for the conventional compliant hinges. This range is also determined analytical, based on the material properties Practically this range could differ from the analytical results due to physical limitations, similar to the proposed hinge. The maximum angle of rotation for the proposed hinge does not meet the state of the art angles of rotation. Theoretically, the angle of rotation is proportional to the input force by means of the rotation stiffness of the hinge. In practice the geometric size of the hinge determines the potential angle of rotation. Also inefficiencies in the silicone material could differ the angle of rotation, since the material properties of the silicone could variate due to the composite with the hardener. This varies the stiffness and therefore the range of motion. Even the alignment of the rotation is dependent, as the rotation should be applied along the shortest distance across the surface of the hinge. Otherwise the

boundary conditions of the hinge are exceeded, causing a larger rotation stiffness. This means that further research towards the maximum angle of rotation and the geometric design of the hinge needs to be performed, since the maximum angle of rotation is not fully understood yet.

Analysis during deformation of the compliant hinge showed us errors in the FEM model. These errors were mainly causes by the transition elements between the side curves and the actuated surface of the compliant hinge. Here the finite elements are exposed to large deformations, causing errors in the convergence. The errors cause a limited deformation of 6.25% of the height h of the compliant hinge. Other errors are induced by diverging solutions of the FEM model which comply the FEM tolerance, giving negative traction force values. This indicates that the design of the compliant hinge is not capable of finding the maximum angle of rotation in FEM.

To simplify the calculations we have estimated the development of the fluid inside the hinge. The assumptions made about the properties of the water inside the hinge could be reviewed to make sure that the difference in performance is not induces by a misconception in the behaviour of the fluid. The fluid properties provide a relative high normal stiffness and a relative low rotational stiffness. During the experiments on the demonstrator the pressure of the enclosed water was not observed to variation as the repeated measurement results were nearly similar. This could suggest little or no leakage of water during actuation of the hinge. However, it has to be taken into consideration that the pressure in the hinge could be influenced by the increase in temperature due to fluid friction or by the temperature of the water. Another point of interest is the volume of water inside the hinge. The inside of the compliant hinge could contain some air besides the volume of the applied water, this combination of air en water could cause different measurement results of the traction forces on the compliant hinge. For further research it is recommended to develop a method to check the percentage of water inside the compliant hinge.

When lowering the rotation stiffness and increasing the normal stiffness, the proposed compliant hinge is able to provide a large range of operation. Meaning that the proposed hinge is is able to withstand high compression and compliant rotations. The material used to obtain these compliant hinge properties is silicone. Silicone is used for its feasibility and material properties, see elongation and bending. We assume that the stiffness induced by the normal- and rotation-displacement are mostly dependent on the elongation- and bending-stiffness of the material. To obtain these results, other materials can been used, for example: Thin flexure spring steel. On the other hand, the feasibility of the corners and bends along the hinge design is questionable. Large term displacement experiments are recommended in order to validate these theories.

The compliant hinge has not been observed to failure while actuated by a prescribed displacement, as the maximal displacement of the FEM model is 6.25% of the height h. For the maximal displacement of 6.25% of the height h in FEM, the demonstrator does not fail. To validate the compliant hinge in this thesis, the limit of failure for the normal- and rotation-displacement does not have to be known. Since the objective is to obtain a relative large normal stiffness and relative low rotation stiffness under deformation. To address the limitations, the shape of the hinge should be reviewed. The current hinge shape does not provide a sufficient FEM model to locate the physical limits of the hinge design. This limitation of the FEM model could also be observed by the development of the strain energy density and the shear stress on the boundary material of the proposed hinge. At the maximum displacement of the FEM model the shear stress and strain energy density on the boundary material did not exceed their material limits, and the stepsize was kept constant. Even though we measured these quantities at the transition line from the side curves to the front and back plane of the hinge. Here the highest surface stress is indicated during deformation. Therefore the FEM model does not meet the failure identification of the proposed hinge.

The 3D FEM analysis has overestimated both stiffness profiles by approximately $\pm 10\%$ for a displacement of 6.25% of the height h. This could be caused by the wrong assumptions made in the FEM analysis, manufacturing errors in the test setup or even errors in the joint connector. Most likely the composition of the silicone material is not similar to the composition of the silicone material used in the test specimens that obtained the material properties of the silicone. This resulted in larger normal

forces and larger rotation forces than has been assumed by the 3D FEM analysis. This statement applies for both configurations. However, multiple factors could influence the traction forces on the demonstrators, as we should also keep in mind the stick-slip for the contact regions of the joint connector and the silicone material. Throughout this discussion multiple factors are reviewed.

The performance of the hinge decreases when the geometric scale increases. The model predicts a large decrease in performance for an enlargement of the geometry, while for scaling in depth the performance scales constant. The mathematical model for both scaling methods was derived using FEM and is verified by the correlation of the FEM and measurements on the demonstrator. Moreover, the stiffness magnitudes of the 2D hinge model suggest that the scaling in depth provides the traction force regarding the desired depth of the hinge. As mentioned before, the traction forces of the 2D FEM greatly differs from the traction forces of the 3D FEM. The difference in magnitude is probably induced by the small inner volume and the lack of bending stiffness of the 2D hinge design.

Furthermore, for a large length l the surface of the corner spheres is relative small compared to the total surface of the hinge, and therefore the contribution of the corners on the behaviour of the hinge will be inherent smaller, confirming the design choices made in a previous section.

5.2. Appendices

The raw measurements results of the normal traction force and the rotation traction force on the selected surface of the compliant hinge are presented in appendix B.1. The measurements show that the results on the demonstrator are in good correlation with the results of the FEM. However, the development of the traction forces regarding the measurement results of the aluminium connector seem more gradually (Appendix B.2). As the measurement results of the joint connector shows a fluctuation in the development of the traction forces. The measurement results on the aluminium connector are far more stable compared to the measurement results on the joint connector. However, the connection between the hinge and aluminium connector is not sufficient for rotations, because the entire actuated surface of the aluminium connector is not bonded to the surface of the compliant hinge for the complete deformation, inducing a semi rigid actuated surface, see Appendix A.1. If we look further at these measurement results, we find that there is a difference in the normal force on the joint connector and the normal force on the aluminium connector. The development of the normal force on the joint connector induces a low constant magnitude at the start of the measurement. Whereas the slope of both graphs seems similar towards the end of the measurement. The low normal force may be induced by the a small gap between the hinge and joint connector or air inside the hinge, as for a larger preload this problem is solved. The traction forces on the joint connector and on the aluminium connector show a recurrent pattern for both deformations. An undesired deformation of the joint connector could therefore be excluded.

Furthermore the extended test on the demonstrator showed us that a prescribed normal displacement of 17.5% of the height h could also be applied without failure of the hinge. Confirming that the hinge could be compressed for larger displacements. It looked like the compliant hinge could deal with larger deformations, as in the behaviour and traction forces there were no deviations. The measurement results of this test are shown in Appendix B.3. The begin of the plot showed a non-linear development of the normal force. The non-linear normal force could be induced by the a gap between the aluminium connector and compliant hinge, as the additional volume of water provided a curved front and back plane of the compliant hinge. The aluminium connector was located on top of this curve, without preload. Therefore, the non-linear traction force, represented in the plot, is the compression on the curves surface of the hinge, acting like a preload.

The finite element analysis presented in appendix C.1 indicates the Von Mises stress on the surface of the hinge. The Von Mises stress is solely used to obtain the indicate the stress on the boundary material relative to other stress on the compliant hinge. One could see that the stress is equally divided on the side curves of the compliant hinge throughout the normal deformation. The stress on the surface of the corner spheres is relative low to the stress on the side curves. For the rotation the Von Mises stresses are divided more equally over the total surface as the volume inside the hinge is shifted instead of locally increased. This means that the deformation is performed over a large surface, resulting in

lower stresses inside the material and more efficient energy translocation.

According to the measurement results seen in this Appendix, the physics on the demonstrators are similar to the FEM. This is confirmed by the observed line symmetry through the center of the hinge, the symmetry distributes the prescribed displacement over the front- and back-plane of the compliant hinge. However, for the applied moment on the demonstrator the vertical plate slides along the actuated surface of the compliant hinge, whereas the applied moment in FEM is provided by a static load. This could suggest alignment errors, causing performance variation in the measurement results. The slip could imply that the experimental setup has influenced the rotation stiffness of the compliant hinge. Experiments actuated for a pure rotation could be examined to test this theory.

6

Conclusions and Recommendations

The main objective of this research is to improve the performance of the conventional compliant hinge by introducing a new hinge design. This goal is successfully accomplished on the basis of the results presented in Chapter 4. A new type of compliant hinge, which utilizes incompressible fluid inside an elastic closed body to obtain the desired stiffness profiles, is developed and presented in this paper. It is experimentally validated that the performance of the demonstrator corresponds to the performance of the 3D FEM model. The first part of this Chapter summarises the most important conclusions of this thesis project. In the second part recommendations, ideas and tips for further research are given.

6.1. General conclusion

6.1.1. Paper

- The compliant hinge has a larger range of operation than the conventional compliant hinges, as the difference between the normal- and rotation-stiffness exceeds the stiffness ratios of the conventional compliant hinges. The design space of the compliant hinge and conventional compliant hinges are similar.

- The objective of this thesis is achieved, since the performance of the proposed compliant design is at least a factor 30 higher than the best performing conventional hinge G. The stiffness are obtained for a limitation in the displacement of the hinge for 6.25% of the height h.

- Numerical errors mainly depends on the transition elements between the side curves and the actuated surface of the compliant hinge. Here, finite elements are exposed to relative large deformations, causing errors in the convergence of the simulation.

- By introducing the FEM method to validate the demonstrator, the maximal displacement of the FEM model is 6.25% of the height h. For the maximal displacement of 6.25% of the height h of the compliant hinge, the hinge does not fail.

- The load capacity and maximum angle of rotation are not determined as the maximum displacement of the hinge in FEM is used as benchmark. However, further research towards the maximum angle of rotation, load capacity and the geometric design of the hinge are recommended.

- The normal- and rotation-stiffness of the proposed hinge could be designed towards a required magnitude. As many variables influence the stiffness of the hinge, we could adjust these variables towards a required value.

37

- The elongation stiffness of the boundary material is mostly dependent of the normal stiffness of the hinge, while the bending stiffness of the material is mostly dependent on the rotation stiffness of the hinge.

- Any variation to the initial shape of the hinge induces an internal pressure increase that elongates the boundary material to compensate for the decrease in volume causes by the actuated force. The volume inside the hinge is kept constant.

- We assume little or no leakage of water during deformation of the hinge, as the measurements results around the initial geometry of the compliant hinge remain similar.

- The performance of the compliant hinge decreases when the geometry of the hinge is scaled to a larger extent.

- The performance of the compliant hinge decreases when the applied rotation is not aligned along the shortest distance across the surface of the hinge. When the rotation is misaligned on the surface of the hinge, the distance to the middle of the compliant hinge is larger. A larger arm applies a larger moment, upon which the rotation stiffness increases and the performance inherent decreases.

6.1.2. Appendices

- After the compliant hinge is actuated for a prescribed displacement, the deformation is largely divided over a large surface of the boundary material. This results in a lower peak stress and a more efficient energy translocation.

- The measurements results show that the demonstrator and FEM are close correlated. The magnitudes of the curve fitted traction forces at the end of the prescribed displacement are within 1% variation for both deformations.

- The material properties of the joint connector and the silicone material within the joint connector, correspond to the simulated rigid surface in FEM, as the measurement results of the aluminium connector were in close correspondence to the measurements on the joint connector.

- For the measurements of the rotation force on both configurations, the applied moment causes the vertical plate to slides along the surface of the demonstrator. For the applied rotation the aluminium connector provides a smoother development of the traction forces than the joint connector.

6.2. Recommendations

First some recommendations for possible research subjects are given. Next, recommendations for improving the experimental test setup are provided. Finally, an overview of interesting potential applications for the compliant hinge is presented.

6.2.1. Research

- Perform experiments on the maximum angle of rotation and the load capacity of the proposed hinge.

- Perform a general shape optimization to enhance the angle of rotation and the load capacity of the hinge.

- Create more insight in the cause of failure for the proposed hinge.

- Apply a high load to the compliant hinge, causing the hinge to fail. On the failure of the compliant hinge we could learn more about the working principles on deformation.

- Optimising the initial shape of the hinge while obtaining a larger performance within the boundary conditions.

- Model the optimised shape of the compliant hinge without a direct boundary between the actuated surface and the deforming surface to prevent numerical errors.

- Investigate the influence of other fluids inside the compliant hinge. Even a mixture of multiple fluids could be examined.

- Investigate the performance of a high and a low initial pressure inside the compliant hinge.

- Implement the compliant hinge inside static entities, in order to maintain the bending stiffness and increase the compliant characteristics of the entity.

- Investigate the decrease of the performance for geometric scaling on the demonstrator. Also the performance for scaling in depth should be investigated on the demonstrator.

- Create more insight in the degradation process of the compliant hinge over time.

- Investigate the influence of air inside the hinge, as the hinge would not entirely be filled with water.

- Investigate the influence of other boundary material on the hinge, obtaining both stiffness profiles.

- Analyse the presence of stick-slip in the contact regions of the silicone material and the joint connector on deformation.

6.2.2. Experimental test setup

- Set up a method to measure the angle of rotation and the load capacity of the compliant hinge.

- Implement a method to apply a pure rotation on the demonstrator. By doings so, the specific rotation stiffness of the hinge could be calculated without compression of the total hinge.

- Investigate further long term experiments in order to determine the operation time of the hinge before failure.

- Create a measurement setup to gain more insight in the distribution, velocity and the pressure of the fluid inside the hinge during deformation.

- Design a universal measurement setup that applies unproportional shaped surfaces to the surface of the compliant hinge to indicate the behaviour of the compliant hinge for various deformations.

- Design a method to indicate the total compression of the compliant hinge by the applied rotation performed in this thesis.

6.2.3. Potential applications

- The implementation in conventional systems which require large deformable properties for large compressible stiffness, including: Hydrostatic bearings, force distribution system and moving general architecture, including stadium doors [52],[53],[54].

- Implementation in application with face unproportional shaped surfaces, needing a large deformable guiding device to follow the trajectory of the surface while carrying a load.

- Applications which require a compliant hinge for high axial stiffness.

- Applications which require a compliant joint for high axial stiffness, as the proposed hinge could deform around multiple axis.

- General application for high precision compliant hinges and joints.

Appendices

A
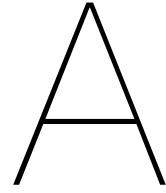
Experimental Test Setup

In this appendix additional information on the experimental test setup, measurement results and the constructed parts and extended datasheets of the paper are provided.

A.1. Overview setup

A picture taken of the experimental test setup can be seen in Figure A.1.
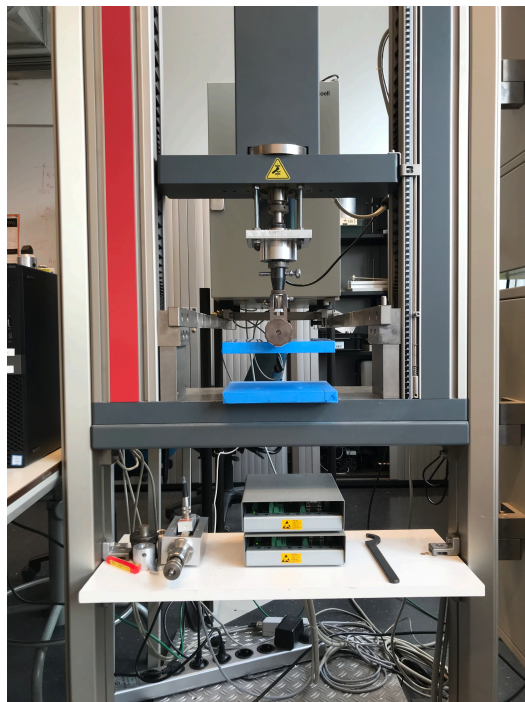
Figure A.1: Total overview of the test bench (Zwick-Roell Z005) and two horizontal plates. These plates are coloured blue to clarify the contrast with the surroundings.

Figures A.2 and A.3 give an overview of the experimental test setup regarding the aluminium connector.

(a)   (b)
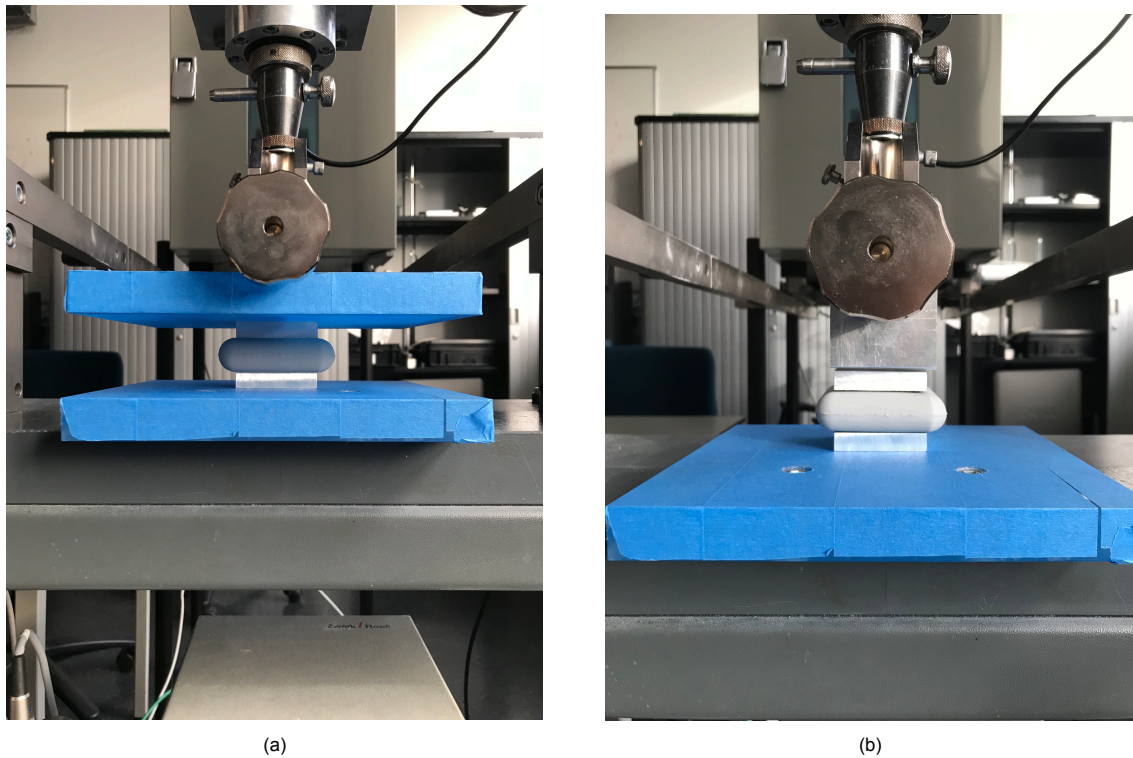
Figure A.2: An overview of the experimental test setup were the proposed hinge is actuated by the aluminium connector. (a) The normal displacement on the compliant hinge provided by two horizontal plates actuated on the aluminium connector. (b) The angular displacement on the compliant hinge provided by a horizontal bottom plate and a vertical top plate actuated on the aluminium connector.
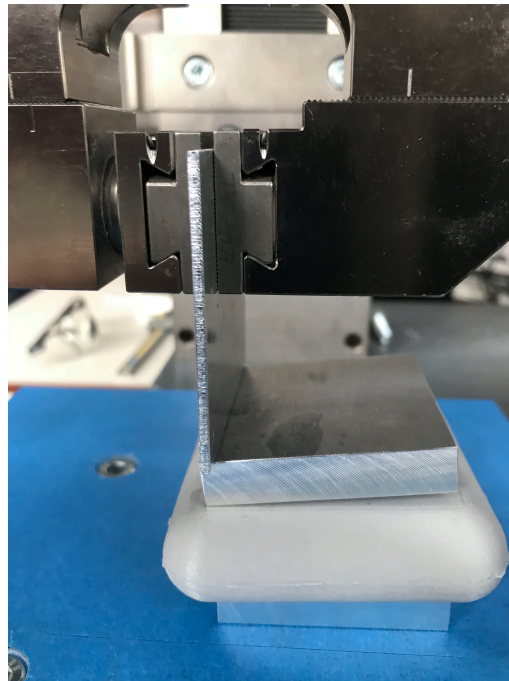
Figure A.3: An extensive side-view of the experimental test setup for rotational deformation provided by a horizontal bottom plate and a vertical top plate actuated on the aluminium connector

A.2. Dimensions of 3D-printed parts

Most of the structural parts of the experimental test setup consist of $3mm$ thick 3D printed PLA material. Figures A.4 till A.5 show the most important dimensions of the structural parts of the joint connector that have been 3D printed for the experimental test setup.

(a)   (b)
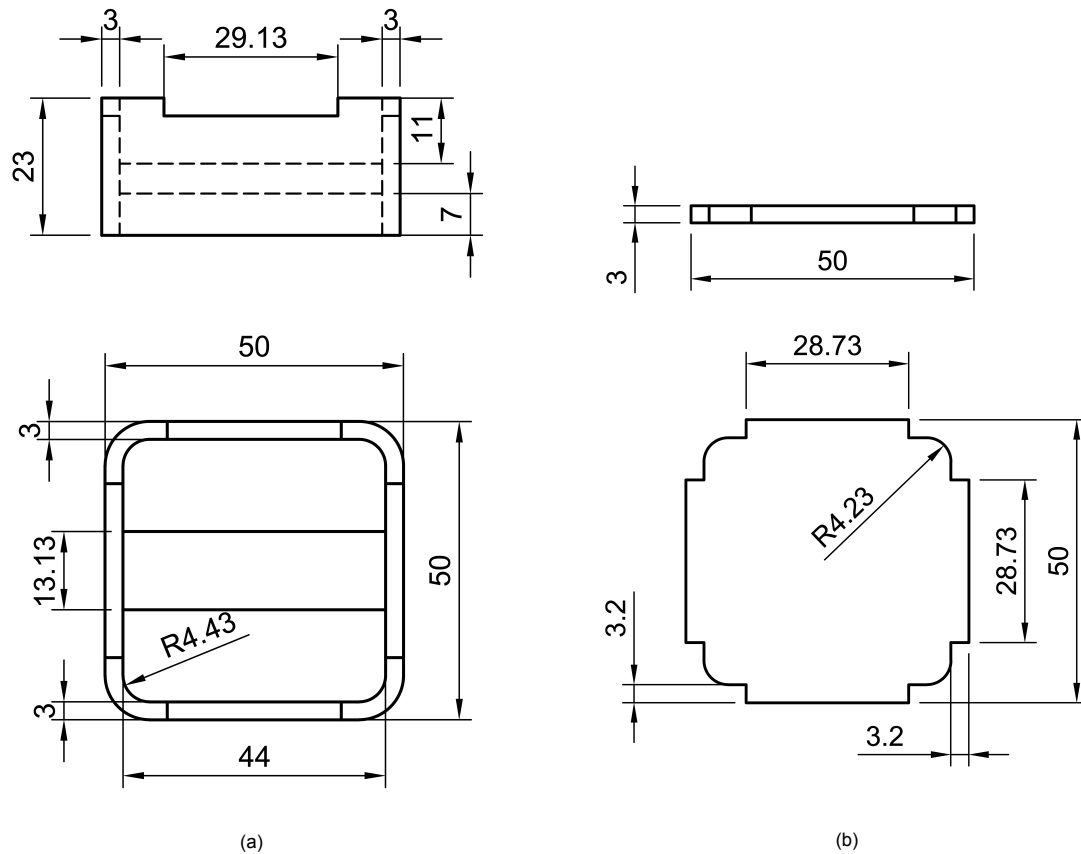
Figure A.4: Drawing of side- and top-view of all parts regarding the joint connector. (a) The dimensions of the base of the joint connector. (b) The dimensions of the lid of the joint connector.

Figures A.6 shows on the left a drawing of the dimensions of the compliant hinge mold. The mold forms the base to shape the compliant hinge by the silicone material. On the right the mold for the specimen of the the tensile strength test is shown.
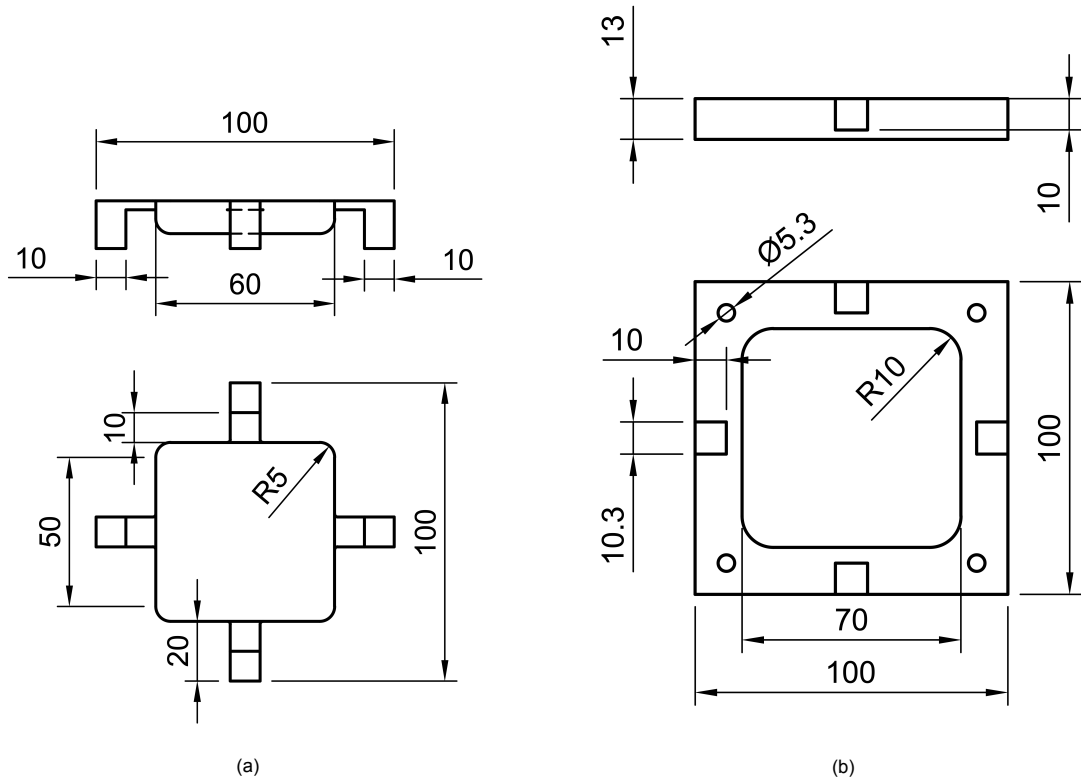
Figure A.5: Drawing of side- and top-view of top and bottom part of the hinge mold. (a) The dimensions of the top part of the hinge mold. (b) The dimensions of the bottom part of the hinge mold. Together these parts could be used to form half of the compliant hinge shape.
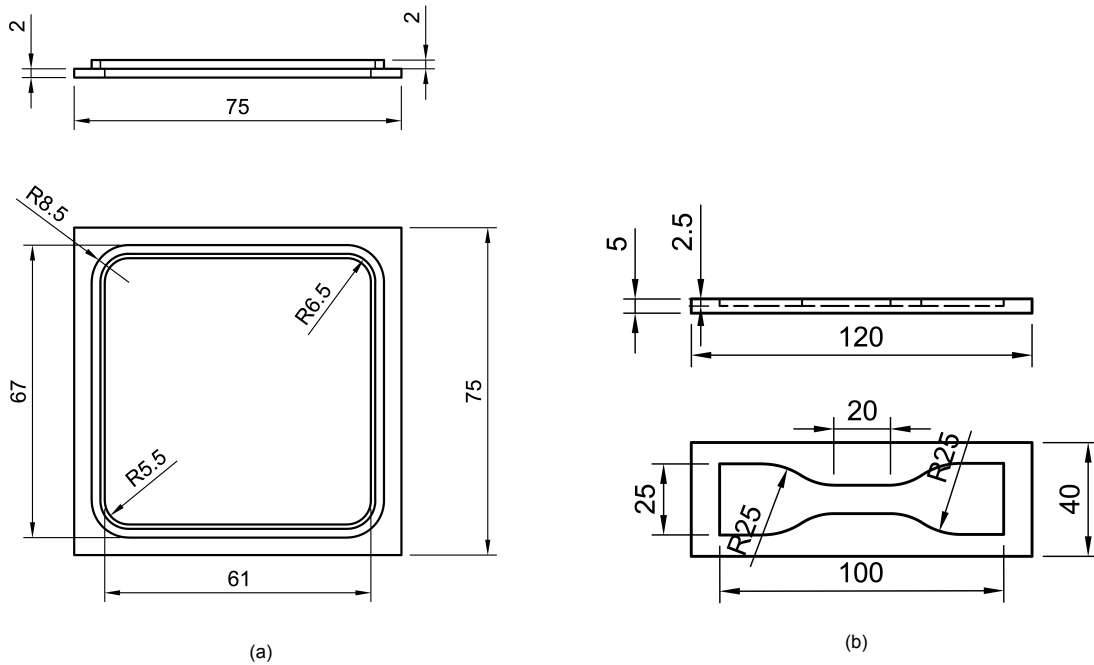
Figure A.6: Drawing of side- and top-view of: (a) The dimensions of the middle part of the hinge mold, introducing a dent in one half of the hinge shape. (b) The dimensions of the mold of the specimen, used for the tensile strength tests to obtain its material properties.

B

Measurement

This appendix provides the data that has been obtained by the experiments done in the paper (Chapter 4). The additional measurements on the traction forces on the proposed hinge are presented.

B.1. Joint connector

Figures B.1 and B.2 present the measurement results of the traction forces on both demonstrators during deformation. The proposed hinge is connected to the testing machine by the joint connector. Each measurement was repeated three times to obtain the correct results.
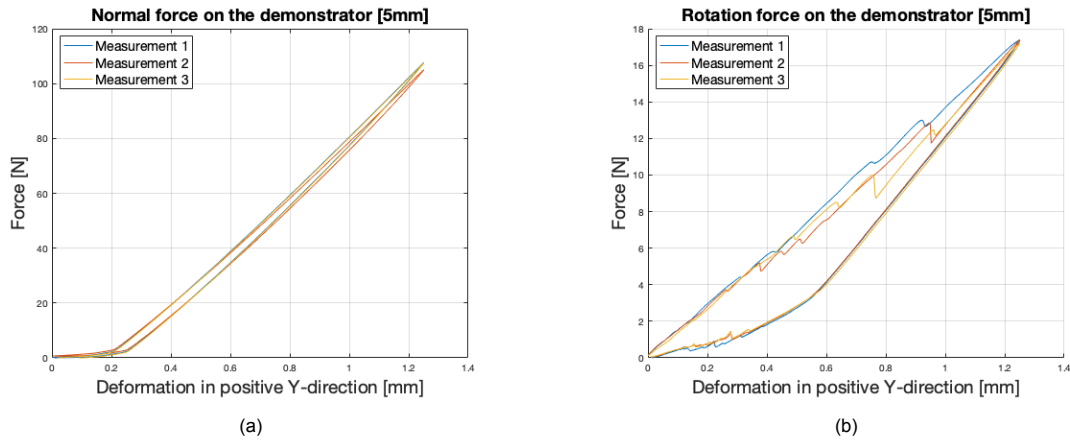
Figure B.1: Plots of all the measurements performed on the first configuration of the demonstrator by the joint connector. The plots show the integrated traction force over the surface of the actuated surface of the hinge. (a) The traction force of the normal displacement. (b) The traction force of the angular displacement. The traction forces are obtained for a displacement of 6.25% of the height h of the demonstrator.
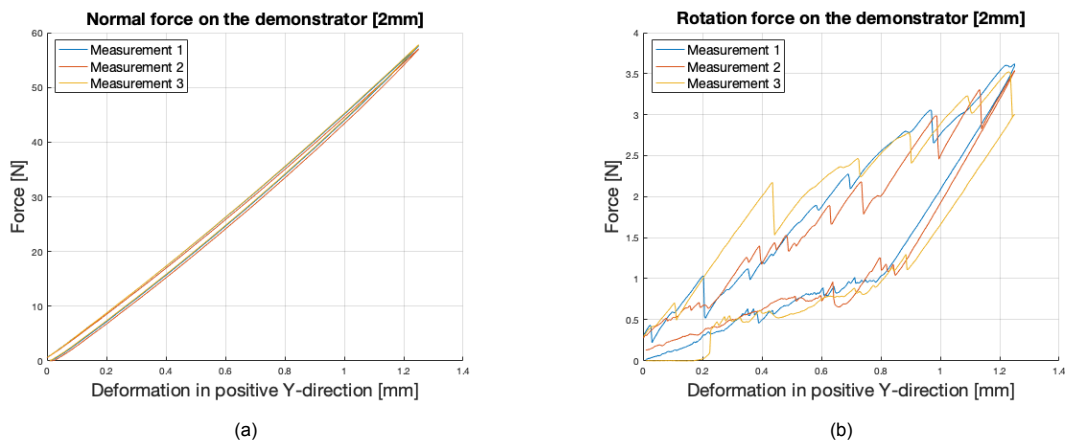
Figure B.2: Plots of all the measurements performed on the second configuration of the demonstrator by the joint connector. The plots show the integrated traction force over the surface of the actuated surface of the hinge. (a) The traction force of the normal displacement. (b) The traction force of the angular displacement. The traction forces are obtained for a displacement of 6.25% of the height h of the demonstrator.

B.2. Aluminium connector

Figure B.3 presents the measurement results of the traction forces on both demonstrators during deformation. Whereas the proposed hinge is connected to the testing machine by the aluminium connector. Each measurement was repeated three times to obtain the correct results.
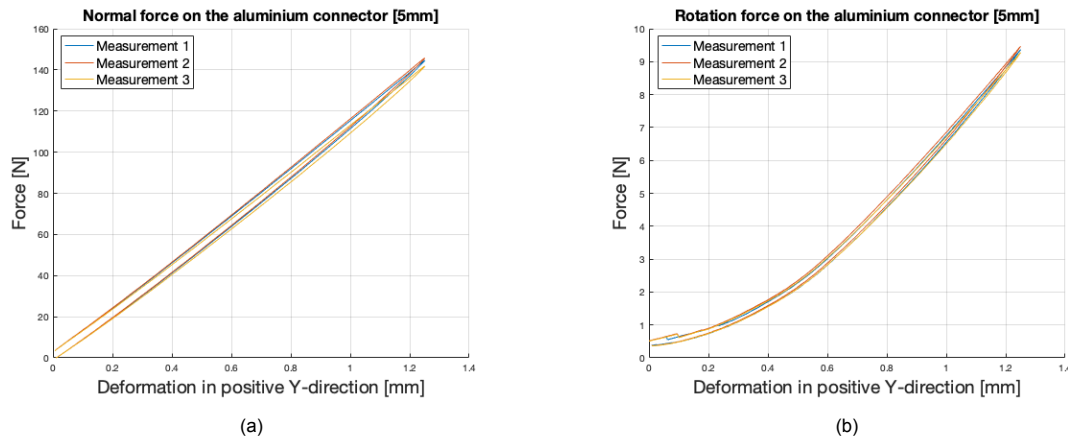
Figure B.3: Plots of all the measurements performed on the first configuration of the demonstrator by the aluminium connector. The plots show the integrated traction force over the surface of the actuated surface of the hinge. (a) The traction force of the normal displacement. (b) The traction force of the angular displacement. The traction forces are obtained for a displacement of 6.25% of the height h of the demonstrator.

B.3. Extended measurement

Figure B.4 present the extended measurement results of the normal forces on the second configuration of the demonstrator. The proposed hinge is connected to the testing machine by the aluminium connector. The measurement is repeated one time.
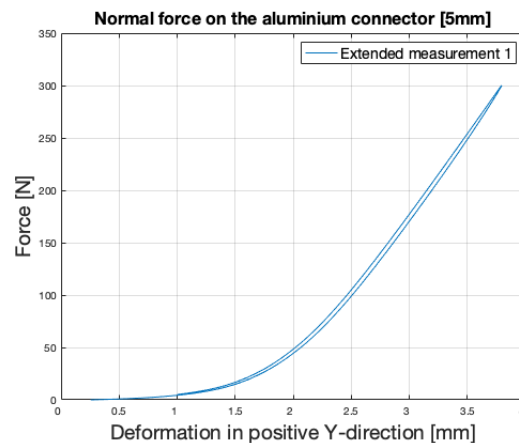
Figure B.4: Plots of the extended measurement performed on the first configuration of the demonstrator by the aluminium connector. The plots show the integrated traction force over the surface of the actuated surface of the hinge for the normal displacement. The proposed hinge is actuated by a displacement of 17.5% of the height (h) of the demonstrator.

C
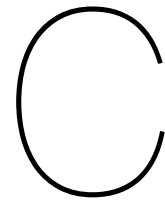
Design notes

C.1. FEM analysis

Figures C.1 and C.2 show the Von Mises stress on the surface of the proposed hinge during normal displacement. The magnitude of the Von Mises stress is in this case irrelevant, since the distribution of the stress during deformation on the hinge is of interest. The mutual difference between the Von mises stress on the surface of the hinge indicates the diffusion of the stress over the boundary material.
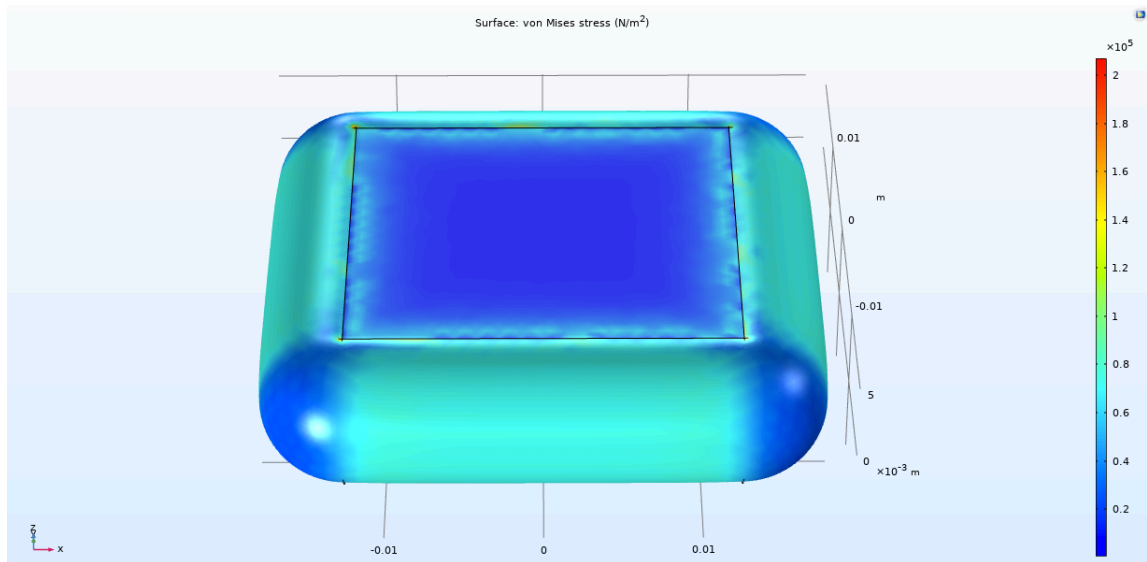
Figure C.1: Schematic side-view of the 3D hinge design for a normal displacement showing the Von Mises stress [$\frac{N}{m^2}$] on the outer surface of the hinge. The Von Mises stresses are obtained for a displacement of 6.25% of the height h of the demonstrator.
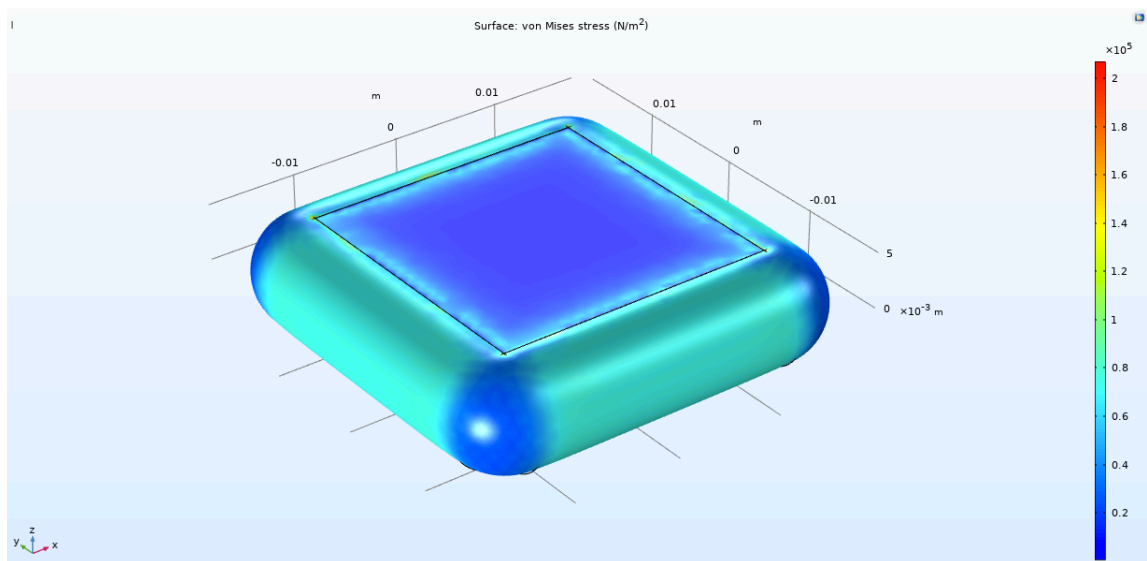
Figure C.2: Schematic isometric-view of the 3D hinge design for a normal displacement showing the Von Mises stress [$\frac{N}{m^2}$] on the outer surface of the hinge. The Von Mises stresses are obtained for a displacement of 6.25% of the height h of the demonstrator.

Figures C.3 and C.4 show the Von Mises stress on the surface of the proposed hinge during rotational deformation. Again the magnitude of the Von Mises stress is irrelevant, since the distribution of the stress during deformation on the hinge is of interest. The mutual difference between the Von mises stress on the surface of the hinge indicates the diffusion of the stress over the boundary material.
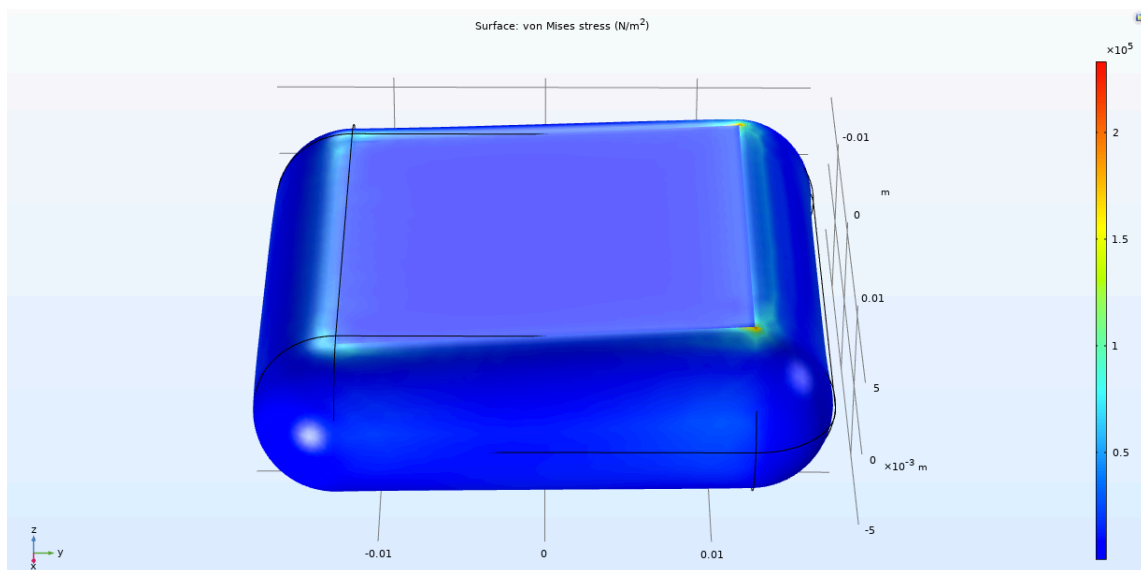
Figure C.3: Schematic side-view of the 3D hinge design for a rotation displacement showing the Von Mises stress $[\frac{N}{m^2}]$ on the outer surface of the hinge. The Von Mises stresses are obtained for a displacement of 6.25% of the height h of the demonstrator.
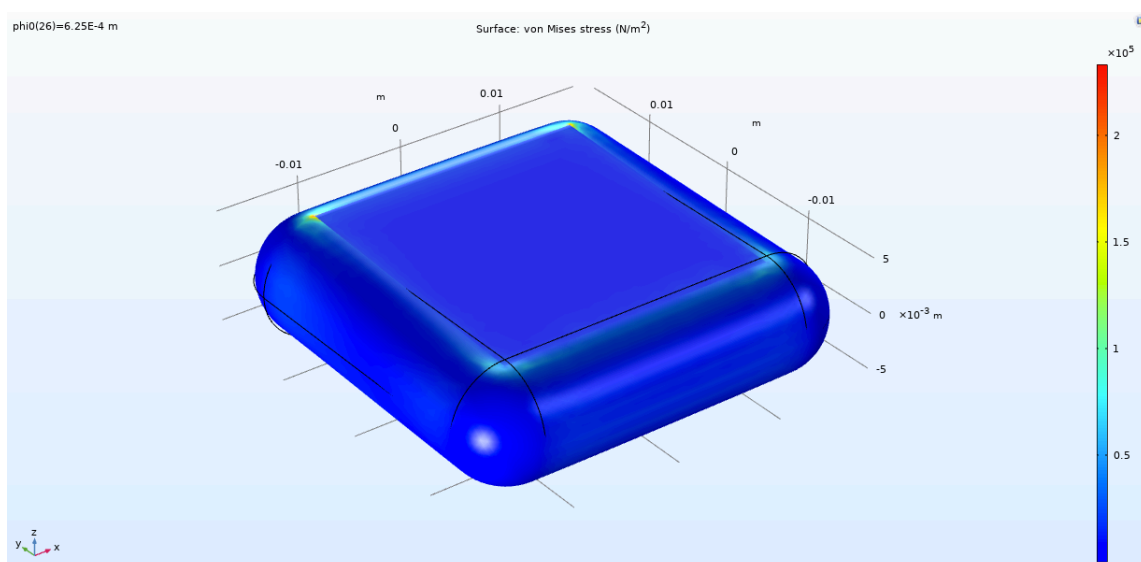
Figure C.4: Schematic isometric-view of the 3D hinge design for a rotation displacement showing the Von Mises stress $[\frac{N}{m^2}]$ on the outer surface of the hinge. The Von Mises stresses are obtained for a displacement of 6.25% of the height h of the demonstrator.

C.2. Conventional hinges

Figures C.5 till C.6 present the visualization and stiffness magnitudes of the conventional hinges as found in literature [28]. From this collection of flexures some hinges are chosen based on their behaviour, as the behaviour is in close correspondence to the behaviour of the proposed hinge.
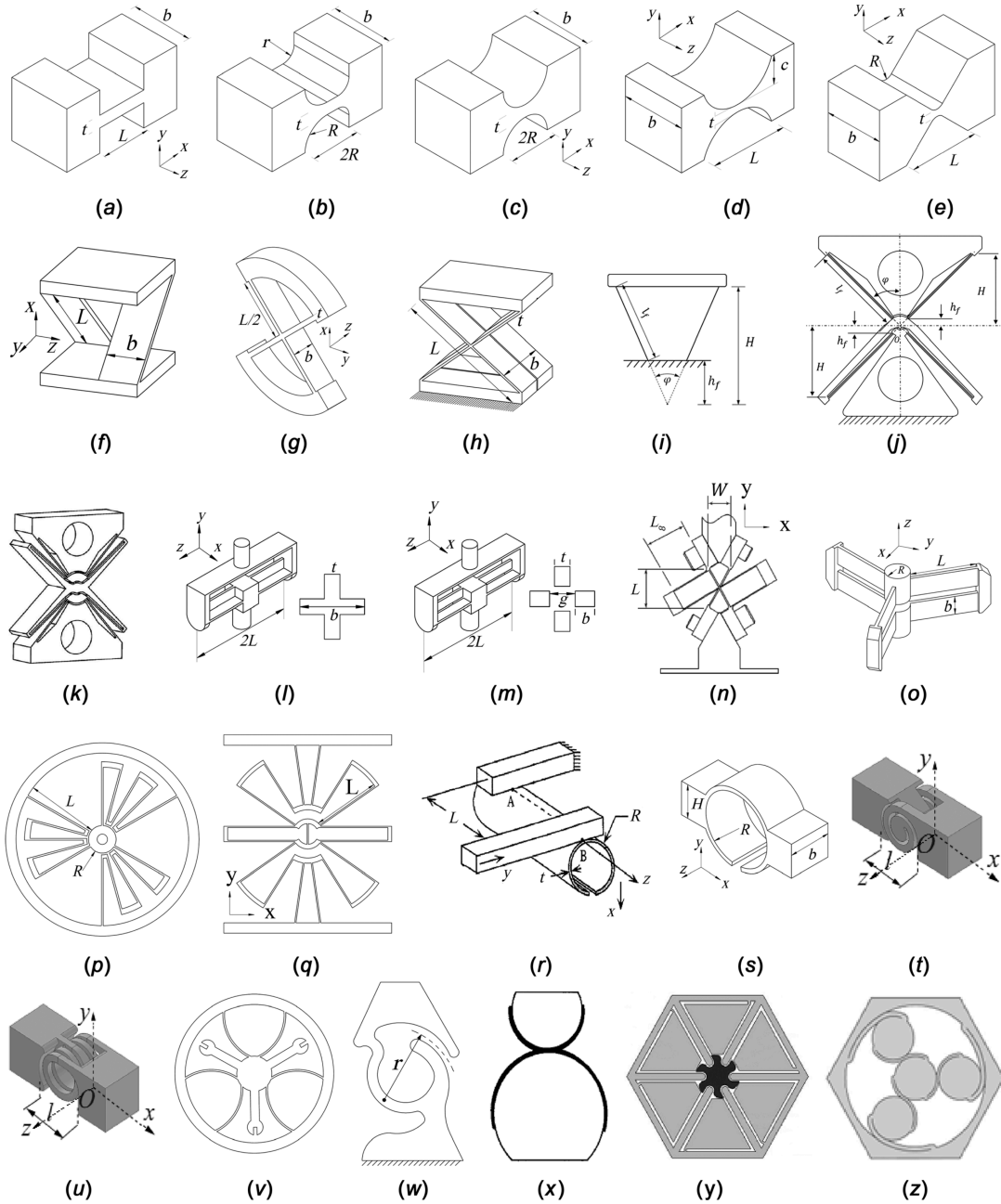
Figure C.5: Compliant revolute joints; (a) rectangular, (b) RCCF, (c) circular, (d) "a" parabolic, "b" hyperbolic, "c" elliptical, "d" cycloidal, (e) V-shape, (f) cross axis, (g) cartwheel, (h) X2, (i) LITF, (j) ADLIF, (k) butterfly, (l) CR-1, (m) CR-2, (n) '-flexure hinge, (o) CR-3, (p) multileaf, (q) multileaf spring, (r) split-tube-1(ST-1), (s) ST-2, (t) spiral, (u) helical, (v) annulus-shape, (w) revolute pair, (x) XR-joint, (y) contact-aided, and (z) rolling contact-2

| Compliant revolute joints | Primitive flexure | Complex flexure | Notch-type | Leaf-spring | Tape-spring | Curve-beam | Contact-base | Range of motion θ_z (rad) | Axis drift δ_z (μm) | $K_{\theta z}$ | $K_{\theta y}$ | $K_{\theta x}$ | K_z | K_y | K_x |
										N·mm/rad × 10⁻³			N/mm × 10⁻³		
Fig. 3(a) [36–39]	•		•					0.113	198.7	6.481	648.15	246.1	24	0.24	77.78
Fig. 3(b) [40]	•		•					0.06	4.2	0.112	—	—	—	—	—
Fig. 3(c) [36–39]	•		•					0.03	34	23.342	1267.6	485.33	55.05	1.153	152.11
Fig. 3(d)-a [41,42]	•		•					—	—	20.43	—	—	—	15.53	265.04
Fig. 3(d)-b [41,42]	•		•					—	—	7.103	—	—	—	77.4	164.64
Fig. 3(d)-c [42,43]	•		•					—	—	23.342	1267.6	—	—	57.186	152.11
Fig. 3(d)-d [44]	•		•					—	—	36.12	1832	—	80.66	1.758	109.84
Fig. 3(e) [44]	•		•					—	—	34.142	1585.1	—	68.15	1.642	94.99
Fig. 3(f) [38,45,46]		•		•				1.676	6620	0.0079	5.6	2.11	0.042	0.00006	4.2
Fig. 3(g) [38]		•		•				0.419	82.8	0.0315	22.4	8.433	0.672	0.0009	16.8
Fig. 3(h) [47]		•		•				0.838	130	0.0078	1.4	0.529	0.042	0.0002	4.2
Fig. 3(i) [48,49]		•		•				0.173	34	0.094	11.2	4.22	0.336	0.00047	8.4
Fig. 3(j) [48–51]		•		•				0.346	11.9	0.047	5.6	2.1	0.168	0.00024	4.2
Fig. 3(k) [48–52]		•		•				0.35	—	0.021	2.8	1.054	0.084	0.00012	2.1
Fig. 3(l) [21]		•		•				0.558	0	0.0941	358.52	358.52	33.29	10.76	10.76
Fig. 3(m) [21]		•		•				0.267	0	0.126	89.73	89.73	33.6	2.7	2.7
Fig. 3(n) [53]		•		•				—	—	—	—	—	—	—	—
Fig. 3(o) [21]		•		•				1.4	—	0.0057	—	—	1.01	—	—
Fig. 3(p) [20]		•		•				2.55	—	0.0027	—	—	0.403	—	—
Fig. 3(q) [54]		•			•			—	—	—	—	—	—	—	—
Fig. 3(r) [55,56]	•					•		0.65	—	0.056	82.6	82.6	—	2.48	2.48
Fig. 3(s) [57]	•					•		—	—	—	—	—	—	—	—
Fig. 3(t) [58]	•					•		—	—	—	—	—	—	—	—
Fig. 3(u) [58]	•					•		—	—	—	—	—	—	—	—
Fig. 3(v) [20]		•				•		—	—	—	—	—	—	—	—
Fig. 3(w) [59]	•					•		—	—	—	—	—	—	—	—
Fig. 3(x) [60–62]		•					•	—	—	—	—	—	—	—	—
Fig. 3(y) [63]		•					•	—	—	—	—	—	—	—	—
Fig. 3(z) [64]		•					•	—	—	—	—	—	—	—	—

Table 3 Geometric parameters values for compliant revolute joints

Compliant revolute joint	b (mm)	L, l_f (mm)	t, r (mm)	C, R, g, h_f (mm)	$\varphi, \varphi_1, \varphi_2$ (deg)
Figs. 3(a)–3(d)	10	9	1	4.5	—
Fig. 3(e)	10	9	1	2.25	—
Figs. 3(f)–3(h)	4	20	0.15	—	45
Figs. 3(i) and 3(j)	4	10	0.15	1	45
Fig. 3(k)	4	10	0.15	1	40, 50
Fig. 3(l)	8	10	0.15	—	—
Fig. 3(m)	4	10	0.15	0.2	—
Figs. 3(o) and 3(p)	4	10	0.15	2	—
Fig. 3(r)	—	10	0.15	3	—

Figure C.6: Overview of the compliant revolute joints, with flexure type, range of motion, axis drift, on-axis and off-axis stiffness; Dash (-) denotes the analytical data are not available. The embodiment of each hinge is showed in Figure C.5

D
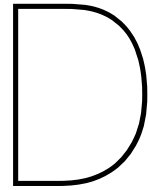
Datasheets

Section D.1 presents the material specifications of the silicone material. Including the concerned website.

Section D.2 presents the specification of the fluid. The water was tapped from the pipe entering my house. The specification are published by the supplier of the tap water for the 4th quarter of 2019.

Section D.3 presents the specifications of the Zwick-Roell Z005 machine. The detailed product information provides the applications and limitations of the machine.

D.1. Material specifications

SILICONENRUBBER PS 8540 SET

bestaat uit Poly-Sil PS 8540 Siliconenrubber A en B component

Maat:

Kleur:

€ 72.12 incl. BTW

1

✓ Voor 15.00 uur besteld vandaag verzonden

✓ Beveiligde betaalomgeving via SSL!

✓ Afhalen in Amsterdam of Nieuwerkerk a/d IJssel

☰   🔍   👤   🛒

Mengverhouding	Meng 100 gewichtsdelen A met 100 gewichtsdelen B
Verwerkingstemperatuur	Minimaal 15°C
Verwerkingstijd	Bij 20°C circa 15 minuten
Ontvormbaar	Bij 20°C na circa 2 uur
Kleur	Wit / Grijs
Maat	2 kg,10 kg,20 kg,30 kg,40 kg,50 kg
Type	PS 8540
Opslag	Koel, droog en vorstvrij bewaren

13 ANDERE PRODUCTEN IN DEZELFDE CATEGORIE:

SILICONENOLIE
€ 11.86
MEER

PRAKTIJKHANDBOEK
€ 29.89
TOEVOEGEN AAN WINKELWAGEN

SILICONEN VERDIKKINGSMIDI
€ 7.26
MEER

PRODUCTEN VAN HETZELFDE MERK

D.2. Fluid specifications

HET WATERLABORATORIUM

Gegevens 4e kwartaal 2019 Dunea

Locatie: **Katwijk**
Naam: **Rein water**

Omschrijving	Eenheid	meetgegevens			norm Drinkwaterbesluit	
		minimum	gemiddelde	maximum	min	max
Aluminium	µg/l Al	3,4	3,4	3,4		200
Arseen	µg/l As	3,1	3,4	3,7		10
Boor	mg/l B	0,05	0,05	0,05		0,5
Calcium	mg/l Ca	39	40	41		-
Chloride	mg/l Cl	49	51	53		150 **
Koolstofdioxide	mg/l CO_2	0,6	0,7	0,9		-
EGV (elek. geleid.verm. 20°C)	mS/m	47,9	48,7	49,6		<125
Fluoride	mg/l F	0,21	0,22	0,24		1,0
IJzer	mg/l Fe	<0.01	<0.01	<0.01		0,2
Troebeling	FTU	<0.03	0,05	0,20		1
Geur (kwalitatief)		afwezig	afwezig	afwezig		****
Waterstofcarbonaat	mg/l HCO_3	169	170	173	>60	
Kwik	µg/l Hg	<0.02	<0.02	<0.02		1
Totale hardheid	mmol/l	1,28	1,33	1,36	>1.0	
Totale hardheid	°Duits	7,2	7,4	7,6	>5.6	
Kleurgetal	mg/l Pt	5	5	6		20
Lood	µg/l Pb	<0.5	<0.5	<0.5		10
Magnesium	mg/l Mg	7,6	7,8	8,0		-
Mangaan	mg/l Mn	<0.01	<0.01	<0.01		0,05
Natrium	mg/l Na	56	57	59		150
Ammonium	mg/l NH_4	<0.02	<0.02	<0.02		0,2
Nitriet	mg/l NO_2	<0.007	<0.007	0,008		0,1
Nitraat	mg/l NO_3	1,71	2,42	3,03		50
Zuurstof, opgelost	mg/l O_2	9,3	9,3	9,3	>2	
pH berekend	pH	8,43	8,55	8,62	7,0	9,5
Orthofosfaat	mg/l PO_4	0,18	0,18	0,18		-
Seleen	µg/l	<0.5	<0.5	<0.5		10
Verzadigingsindex S.I. berekend	pH	0,82	0,82	0,82	> -0.2	
Smaak (kwalitatief)		afwezig	afwezig	afwezig		****
Sulfaat	mg/l	44	46	47		150
Temperatuur	°C	14,1	15,3	16,5		25
Totaal organisch koolstof	mg/l	2,1	2,1	2,1		****
Aeromonas	kve/100 ml	0	1	1		1000
Clostridium perfringens	kve/100 ml	0	0	0		0
Coli 37°C	kve/100 ml	0	0	0		0
Enterococcen	kve/100 ml	0	0	0		0
Koloniegetal 22 °C *	kve/ml	2	2	3		100 ***
Legionella	kve/l	<50	<50	<50		<100

* Geometrisch kwartaalgemiddelde koloniegetal 22°C = 2.3

** norm jaargemiddelde
*** norm geometrisch jaargemiddelde

D.3. Testing machine specifications

Zw*i*ck / **Roell**

Product Information
ProLine table-top testing machines Z005 up to Z100

ProLine Z050TN
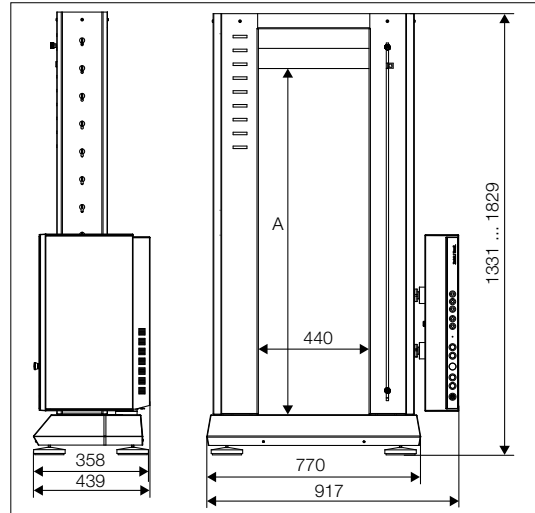
Principle drawing of the ProLine Z005/Z020 TN

Range of application
The ProLine materials testing machine product group was primarily developed for standardized tests on materials and components. Used in conjunction with the intuitive testXpert II software, ProLine materials testing machines are fast and very easy to operate.

Made in Germany
ProLine, including all mechanical, electronic and software components, together with the extensive range of accessories are developed and produced at Zwick Roell's production facility in Germany and are therefore ideally matched to each other. This means that ProLine is an extremely high-quality product and also allows Zwick to offer the best possible support.

Powerful drives
Extremely low minimum speeds can be set, combined with excellent speed-accuracy. The drive also delivers high crosshead travel resolution; this is important in tests on components requiring a high degree of travel-precision and in tests on specimens with high levels of stiffness and low travel, for example.

The high test speed range can be used without restriction. In addition, test loads up to 110% of the machine nominal load are permissible to compensate for heavy combinations of test fixtures, accessories etc.

The faster return speeds reduce cycle times and increase test throughput, with AC drive technology ensuring that the motor is maintenance-free.

Precision crosshead guides
ProLine's moving crosshead is guided very accurately via two steel columns, enabling precise force application to the specimen. This is advantageous for flexure, tests, compression tests, precision tests on components etc.

Exclusively from Zwick: Xforce load cells
ProLine materials testing machines are equipped with Xforce load cells developed and manufactured in the Zwick Roell Group. The effect of parasitic influences (such as temperature and transverse forces) on test results is significantly less than with other, comparable load cells. In addition, Xforce loads cells are very stable and less sensitive to transverse forces in compression and flexure tests, for example.

Short delivery times
The very short delivery time of 2 weeks for ProLine materials testing machines means that pending tests can quickly be tackled without losing valuable time.

Safety for you and the entire testing system
Features ensuring safety include the 2-channel (= double safeguard) safety circuit, operating-mode selector-switch, Drive Off switch and motor holding brake.

Zwick / Roell

Product Information
ProLine table-top testing machines Z005 up to Z100

Powerful, innovative testControl II electronics

ProLine is equipped with testControl II digital measurement and control electronics, mounted vertically on the load frame for better protection against ingress of liquids or conductive particles.

testXpert II – intelligent and reliable
testXpert II testing software and testControl II electronics are perfectly matched, ensuring safe, efficient, reliable operation of the testing machine. testXpert II offers the optimum solution for any testing requirement.

Eco mode
testControl II automatically switches to eco mode when not in use, saving energy.

Built-in safety in accordance with EC Machinery Directive
The statutory safety requirements of the EC Machinery Directive are implemented in all Zwick machines, which are accompanied by an EC Declaration of Conformity on delivery. Only the latest safety technologies and proven industrial components are used. A very high level of safety is guaranteed for user, test results, specimen material and testing system.

Ergonomic remote control with display
The entire test can be performed via the display-equipped remote control unit, independently of the PC. In addition, rapid, high-precision positioning is possible via the rocker switch with integrated thumbwheel.

Overview of key advantages of testControl II electronics

Flexibility through modularity
testControl II provides 6 flexible, time-synchronized slots, enabling several sensors to be in use at the same time, with monitoring and protection, regardless of use.

Machine compliance correction
The high-quality drive technology and on-line machine compliance correction enable extremely accurate travel measurement and positioning.

High data transmission rate
High data transmission rate (2000 Hz) allows fast measurement combined with maximum reproducibility. This is highly advantageous for rapid tests, short brittle fracture events and for tear growth, adhesion and peel tests, for example.

System monitoring
Detailed information regarding current status and usage level of testing equipment greatly simplifies processes such as planning maintenance and spares/replacement procurement.

Fast, adaptive drive-controller
The high drive control frequency of 1000 Hz enables fast, precise force and strain control. Benefits include enabling components to be loaded very quickly and accurately with the specified force.

In addition, all control parameters required for fast, accurate approach to target positions are automatically set, enabling time and cost savings by eliminating the need for time-consuming pre-tests.

Maximum accuracy
High (24-bit) measured-value resolution for maximum test-result accuracy and reproducibility. This means for example that even minimal force changes on the specimen can be recorded and displayed accurately.

Innovative interfaces
E.g. time-synchronised EtherCat® bus system allows future-proof sensor integration to be taken for granted.

Zwick / Roell

Product Information
ProLine table-top testing machines Z005 up to Z100

Data	Value
Load frame	
Finish	RAL 7021 black grey, stainless steel metallic, RAL 3031 orientred
Ambient temperature	+10 ... +35 °C
Air humidity	20 ... 90 %
Conformity	ISO 9000 and CE
Drive system	
Motor	AC servo-motor
Input signal, set-value preset	digital (real-time Ethernet, EtherCAT®)
Controller / Cycle time	adaptive / 1000 Hz
Positioning, repetition accuracy	±2 µm
Permissible feedback energy	Up to 50 % machine utilization
Measurement and control electronics	
Number of slots available for measurement and control modules	2 synchronized module bus slots (expandable to 5)[1] 1 synchronised PCIe slots
Force measurement	grade 0.5 / 1 see load cell, to DIN EN ISO 7500-1, ASTM E4,
Measurement range	up to 165 % of F_N
Calculated resolution (e.g. in tensile / compression direction)	24 bits
Data acquisation rate, internal	400 kHz
Test data transmission rate to the PC	500 Hz (optional 2000 Hz)
Zero-point correction	automatically at measurement begin
Measurement signal runtime correction for all channels	yes
Interface for PC	Ethernet
Eco Mode	yes, power section automatically switched off (time adjustable)
CE conformity	yes, according to machine guidelines 2006/42/EG
Power ratings	
Electrical connections	230 VAC
Range of tolerance	± 10 %
Mains frequency	50/60 Hz

[1] A DCSC module is included in delivery (occupies one module bus slot).

Zwick / Roell

Product Information
ProLine table-top testing machines Z005 up to Z100

| Type | Z005TN | Z010TN | Z010TH[2] | Z020TN | Z030TN | Z050TN | Z100TN | |
Item number	059008	059010	059011	059012	059013	059021	1025089	
Load frame								
Test load F_N in tensile/compr. direction	5	10	10	20	30	50	100	kN
Test area width	440	440	440	440	440	440	640	mm
Height of test area (dimension A)[1]	1070	1050	1450	1050	1370	1370	1360	mm
Max travel of moving crosshead[1]	1000	980	1380	980	1285	1285	1275	mm
Height	1331	1331	1731	1331	1743	1743	1829	mm
Width	770	770	770	770	850	850	1070	mm
Width with electronics console	917	917	917	917	1000	1000	1205	mm
Depth	358	358	358	358	456	456	602	mm
Depth with electronics console	439	439	439	439	462	462	645	mm
Total weight with electron. console	110	135	150	135	330	330	530	kg
Lower mounting stud dia. (included in scope of supply)	20	20	20	36	36	36	60	mm
Noise level measured at maximum test speed	59	57	57	58	68	69	60	dB (A)
Drive unit								
Crosshead speed $v_{min} \dots v_{Nenn}$	0,0005 ... 1500	0,0005 ...1000	0,0005 ...1000	0,0005 ... 500	0,0005 ... 300	0,0005 ... 600	0,0005 ... 300	mm/min
Increased crosshead return speed (at reduced force)	2000	1500	1500	750	500	800	400	mm/min
Drive system's travel resolution	0.039	0.038	0.038	0.018	0.012	0.016	0.0081	µm
Positioning, repetition accuracy	± 2	± 2	± 2	± 2	± 2	± 2	± 2	µm
Power ratings								
Electrical connections (adjustable)	1 PH, N, PE							
Mains frequency	50/60	50/60	50/60	50/60	50/60	50/60	50/60	Hz
Power rating	0.8	0.8	0.8	0.8	0.8	1.6	1.6	kVA

[1 Without accessories
[2 At testing machine Z010 TH the maximum total weight of in the moving crosshead inserted specimen grips and tools is limited to 20 kg

All data at ambient temperature.

Zwick / Roell

Product Information
ProLine table-top testing machines Z005 up to Z100

Data	Value
Load frame	
Finish	RAL 7021 black grey, stainless steel metallic, RAL 3031 orientred
Ambient temperature	+10 ... +35 °C
Air humidity	20 ... 90 %
Conformity	ISO 9000 and CE
Drive system	
Motor	AC servo-motor
Input signal, set-value preset	digital (real-time Ethernet, EtherCAT®)
Controller / Cycle time	adaptive / 1000 Hz
Positioning, repetition accuracy	±2 µm
Permissible feedback energy	Up to 50 % machine utilization
Measurement and control electronics	
Number of slots available for measurement and control modules	2 synchronized module bus slots (expandable to 5)[1] 1 synchronised PCIe slots
Force measurement	grade 0.5 / 1 see load cell, to DIN EN ISO 7500-1, ASTM E4,
Measurement range	up to 165 % of F_N
Calculated resolution (e.g. in tensile / compression direction)	24 bits
Data acquisation rate, internal	400 kHz
Test data transmission rate to the PC	500 Hz (optional 2000 Hz)
Zero-point correction	automatically at measurement begin
Measurement signal runtime correction for all channels	yes
Interface for PC	Ethernet
Eco Mode	yes, power section automatically switched off (time adjustable)
CE conformity	yes, according to machine guidelines 2006/42/EG
Power ratings	
Electrical connections	230 VAC
Range of tolerance	± 10 %
Mains frequency	50/60 Hz

[1] A DCSC module is included in delivery (occupies one module bus slot).

Zwick / Roell

Product Information
ProLine table-top testing machines Z005 up to Z100

Type Item number	Z005TN 059008	Z010TN 059010	Z010TH[2] 059011	Z020TN 059012	Z030TN 059013	Z050TN 059021	Z100TN 1025089	
Load frame								
Test load F_N in tensile/compr. direction	5	10	10	20	30	50	100	kN
Test area width	440	440	440	440	440	440	640	mm
Height of test area (dimension A)[1]	1070	1050	1450	1050	1370	1370	1360	mm
Max travel of moving crosshead[1]	1000	980	1380	980	1285	1285	1275	mm
Height	1331	1331	1731	1331	1743	1743	1829	mm
Width	770	770	770	770	850	850	1070	mm
Width with electronics console	917	917	917	917	1000	1000	1205	mm
Depth	358	358	358	358	456	456	602	mm
Depth with electronics console	439	439	439	439	462	462	645	mm
Total weight with electron. console	110	135	150	135	330	330	530	kg
Lower mounting stud dia. (included in scope of supply)	20	20	20	36	36	36	60	mm
Noise level measured at maximum test speed	59	57	57	58	68	69	60	dB (A)
Drive unit								
Crosshead speed $v_{min} \dots v_{Nenn}$	0,0005 ... 1500	0,0005 ...1000	0,0005 ...1000	0,0005 ... 500	0,0005 ... 300	0,0005 ... 600	0,0005 ... 300	mm/min
Increased crosshead return speed (at reduced force)	2000	1500	1500	750	500	800	400	mm/min
Drive system's travel resolution	0.039	0.038	0.038	0.018	0.012	0.016	0.0081	µm
Positioning, repetition accuracy	± 2	± 2	± 2	± 2	± 2	± 2	± 2	µm
Power ratings								
Electrical connections (adjustable)	1 PH, N, PE							
Mains frequency	50/60	50/60	50/60	50/60	50/60	50/60	50/60	Hz
Power rating	0.8	0.8	0.8	0.8	0.8	1.6	1.6	kVA

[1] Without accessories
[2] At testing machine Z010 TH the maximum total weight of in the moving crosshead inserted specimen grips and tools is limited to 20 kg

All data at ambient temperature.

Zwick / Roell

Product Information
ProLine table-top testing machines Z005 up to Z100

Type Item number	Z005TN 059008	Z010TN 059010	Z010TH[2 059011	Z020TN 059012	Z030TN 059013	Z050TN 059021	Z100TN 1025089	
Load frame								
Test load F_N in tensile/compr. direction	5	10	10	20	30	50	100	kN
Test area width	440	440	440	440	440	440	640	mm
Height of test area (dimension A)[1	1070	1050	1450	1050	1370	1370	1360	mm
Max travel of moving crosshead[1	1000	980	1380	980	1285	1285	1275	mm
Height	1331	1331	1731	1331	1743	1743	1829	mm
Width	770	770	770	770	850	850	1070	mm
Width with electronics console	917	917	917	917	1000	1000	1205	mm
Depth	358	358	358	358	456	456	602	mm
Depth with electronics console	439	439	439	439	462	462	645	mm
Total weight with electron. console	110	135	150	135	330	330	530	kg
Lower mounting stud dia. (included in scope of supply)	20	20	20	36	36	36	60	mm
Noise level measured at maximum test speed	59	57	57	58	68	69	60	dB (A)
Drive unit								
Crosshead speed $v_{min} … v_{Nenn}$	0,0005 … 1500	0,0005 …1000	0,0005 …1000	0,0005 … 500	0,0005 … 300	0,0005 … 600	0,0005 … 300	mm/min
Increased crosshead return speed (at reduced force)	2000	1500	1500	750	500	800	400	mm/min
Drive system's travel resolution	0.039	0.038	0.038	0.018	0.012	0.016	0.0081	µm
Positioning, repetition accuracy	± 2	± 2	± 2	± 2	± 2	± 2	± 2	µm
Power ratings								
Electrical connections (adjustable)	1 PH, N, PE							
Mains frequency	50/60	50/60	50/60	50/60	50/60	50/60	50/60	Hz
Power rating	0.8	0.8	0.8	0.8	0.8	1.6	1.6	kVA

[1 Without accessories
[2 At testing machine Z010 TH the maximum total weight of in the moving crosshead inserted specimen grips and tools is limited to 20 kg

Bibliography

[1] Kota S. Moon, Y. M. Design of compliant parallel kinematic machines. *27th Biennial Mechanisms and Robotics Conference. Montreal*, 5:35–41, 2002.

[2] Oblak J. Jung J. H. Cikajlo I. Veneman J. F. Goljar N. Bizovicar N. Matjacic Z. Keller T. Perry, J. C. Variable structure pantograph mechanism with spring suspension system for comprehensive upper-limb haptic movement training. *J. Rehab. Res. Dev.*, 48(4):317–334, 2011.

[3] Kamei Y. Ishii, C. On servo experiment of a new multi-dof robotic forceps manipulator for minimally invasive surgery. *5th International Symposium on Mechanics and Its Applications*, pages 27–29, 2008.

[4] Shirinzadeh B. Zhan D. et al. Tian, Y. Three flexure hinges forcompliant mechanism designs based on dimensionless graph analysis. *Precision Engineering*, 34(1):92–100, 2010.

[5] L.L. Howell. *Compliant Mechanisms*. Wiley, New York City, New York, 2001.

[6] Thurner P.J. Hansma P.K. Schitter, G. Design and input-shaping control of a novel scanner for high-speed atomic force microscopy. *Mechatronics*, 18(5-6):282–288, 2006.

[7] Hocken R. Simith S.T. et al. Miller, J.A. X-ray calibrated tunneling system utilizing a dimensionally scale nanometer positioner. *Precision Engineering*, 18(2-3):95–102, 1996.

[8] Lee J.J. Choi, K.B. Passive compliant wafer stage for single-step nano-imprint lithography. *Scientific Instruments*, 76(7):1–6, 2005.

[9] W.B. Rowe. *Hydrostatic, Aerostatic and Hybrid Bearing Design*. Butterworth-Heinemann, Oxford, Oxfordshire, 2012.

[10] S. Smith. *Foundations of Ultra-Precision Mechanism Design*. CRC Press, London, 1995.

[11] Tolou N. Sanchez J.G. Herder, J.L. Statically-balanced compliant micromechanisms. *Mikroniek*, 50:20–25, 2010.

[12] Cammarata A. Gabrielli A et al. Callegari, M. Analysis and design of a spherical micromechanism with flexure hinges. *Journal of Mechanical Design*, 131(5), 2009.

[13] N. Lobontiu. *Compliant Mechanisms: Design of Flexure Hinges*. CRC Press, Boca Raton, 2002.

[14] Pfefferkorn H. Christen, G. Nachgiebige mechanismen: Aufbau, gestaltung, dimensionierung und experimentelle untersuchung. *VDI-Berichte*, 1423:309–329, 1998.

[15] Spanoudakis P. Droz S. Myklebust L.I. Onillon E. Henein, S. Flexure pivot for aerospace mechanisms. *European Space Agency*, (Special Publication) ESA SP-524, 2003.

[16] Magleby S.P. Howell L.L. Fowler, R.M. Flex-16: A monolithic large-displacement compliant rotational hinge. *Mechanism and Machine Theory*, 82:203–217, 2014.

[17] Awtar S. Bedewy M. Tawfick S. Hart A.J. Beroz, J. Compliant microgripper with parallel straight-line jaw trajectory for nanostructure manipulation. *ASPE 2011 Annual Meeting*, 52:90–93, 2011.

[18] Chatagny V. Eichenberger Ali. Baumann Henri. Clavel R. Cosandier, F. Optimizing the design of the 13-hinge rectilinear stage for high straightness translation. 2011.

[19] Bertoldi K. Cohen T., Kurzeja P. Architected squirt-flow materials for energy dissipation. *Mechanics and Physics of Solids*, 109:22–33, 2017.

[20] van Ostayen R.A.J. Nijssen, J.P.A. Open form pressure balancing for compliant hydrostatic thrust bearings. pages 3965–3974, 2019.

[21] Diepeveen N. Kempenaar A. Nijssen, J. Development of an interface between a plunger and an eccentric running track for a low- speed seawater pump. 2018.

[22] Comsolmultiphysics® v. 5.3. www.comsol.com.

[23] Matlab v. r2018a. www.mathworks.com/products/matlab.html.

[24] V.J. Katz. The history of stokes's theorem. *Mathematics Magazine*, 52(3):146–156, 1979.

[25] Ryu Y. Saidpour M. Ibrahim, A. Stress analysis of thin-walled pressure vessels. *Modern Mechanical Engineering*, 5:1–9, 2015.

[26] I.S. Liu. *Continuum Mechanics*. Springer, Berlin, Heidelberg, 2002.

[27] Smith D.R. The cauchy stress tensor. in: An introduction to continuum mechanics. *Solid Mechanics and Its Applications*, 22:143–162, 1993.

[28] Tolou N. Herder J.L. Machekposhti, D.F. A review on compliant joints and rigid-body constant velocity universal joints toward the design of compliant homokinetic couplings. *Journal of Mechanical Design*, 137(3):032301, 2015.

[29] Polyservice. Siliconenrubber-ps8540. URL https://www.polyservice.nl.

[30] F. de Buyl. Silicone sealants and structural adhesives. *Adhesion and Adhesives*, 21(5):411–422, 2001.

[31] ISO STANDARD. Iso 37:2017 rubber, vulcanized or thermoplastic — determination of tensile stress-strain properties. URL https://www.iso.org/standard/53023.html.

[32] Corte W. Belis J. Van Lancker, B. Material properties of a structural silicone for linear adhesive glass-metal connections. 2016.

[33] Hwang I. Lee D. Jung, J. Contact pressure and strain energy density of hyperelastic u-shaped monolithic seals under axial and radial compressions in an insulating joint: A numerical study. *Applied Sciences*, 7(8):792, 2017.

[34] Lava P. Debruyne D. Terentjev E.M. Pritchard, R.H. Precise determination of the poisson ratio in soft materials with 2d digital image correlation. *Soft Matter*, 9(26):6037, 2013.

[35] J. Stewart. *Single variable calculus: Early transcendentals*. Thomson Brooks/Cole, Belmont, California, 2016.

[36] Ren J.X. Liu Y. Hao W.Q. Yang J.X. Wang, C. Analysis of silicone rubber elastomer elastic failure in small-size flexible joint at low temperature. *Key Engineering Materials*, 575–576:427–433, 2013.

[37] A.S. Trube. Compressibility of natural gases. *Journal of Petroleum Technology*, 9(1):69–71, 2013.

[38] Dahl N.C. Lardner T.J. Crandall, S.H. *An Introduction to the Mechanics of Solids*. McGraw-Hill Inc., New York City, New York, 1957.

[39] Cerepi A. Marrauld J. Riffaud, J. Characterization and modelling of argillaceous porous medium by compressional and shear acoustic waves. *Studies in Surface Science and Catalysis*, 160: 697–704, 2007.

[40] L.P. Kosevich A.M. Lifshitz E.M. Landau L.D., Pitaevskii. *Theory of Elasticity*. Butterworth-Heinemann, Oxford, Oxfordshire, 2012.

[41] Harris G.L. Jones, F.E. Density of water formulation for volumetric standards calibration. *Journal of research of the National Institute of Standards and Technology*, 97(3):335–340, 1992.

[42] W.S. Slaughter. *The linearized theory of elasticity*. Birkhauser, Bazel, Swiss Confederation, 2002.

[43] F. Kati. Physical properties of silicone elastomers. *Review article*, 50, 2019.

[44] Liu W.K. Moran B. Belytschko, T. *Nonlinear Finite Elements for Continua and Structures*. John Wiley & Sons Ltd., Hoboken, New Jersey, 2006.

[45] Li Y.G. Duan, J. A beam element for geometric nonlinear dynamical analysis. *Advanced Materials Research*, 919–921:1273–1281, 2014.

[46] M. Peksen. *Multiphysics Modelling*. Academic Press, Cambridge, Massachusetts, 2018.

[47] R.F. Steidel. *An Introduction to Mechanical Vibrations*. John Wiley & Sons Ltd., Hoboken, New Jersey, 1971.

[48] Thwaite E.G. Puttock, M.J. Elastic compression of spheres and cylinders at point and line contact. *Commonwealth Scientific and Industrial Research Organization*, 1969.

[49] Bergström J. Bowden, A.E. *39 - Computer Modeling and Simulation of UHMWPE*. William Andrew Publishing, Norwich, New York, 2017.

[50] Papadopoulos P. Lubliner, J. *Introduction to Solid Mechanics*. Springer International Publishing, Swiss Confederation, 2017.

[51] Lascău S. Ardelean Erika. Josan A. Ardelean, M. Surface treatments for aluminium alloys. *IOP Conference Series: Materials Science and Engineering*, 294:12–42, 2018.

[52] R.A.J. van Ostayen. The hydro–support: An elasto–hydrostatic thrust bearing with mixed lubrication. *Tribology International*, 37:607–616, 2004.

[53] Nijssen J.P.A. van Ostayen R.A.J. van Willigen, N.J. Whiffletree-based deforming hydrostatic bearing. 2019.

[54] A. Mahovič. Typology of retractable roof structures in stadiums and sports halls. *Scientific journal*, 3:90–99, 2015.